Silicon Anode Battery for Aviation Applications

Jade Udomkittivorakul

A thesis
Submitted in partial fulfillment of the
requirements for the degree of

Master of Science

University of Washington

2026

Committee:
Jun Liu
Mitchell Kaiser

Program Authorized to Offer Degree:
Materials Science and Engineering

University of Washington

Abstract

Silicon Anode Battery for Aviation Applications

Jade Udomkittivorakul

Chair of the Supervisory Committee:
Jun Liu
Materials Science and Engineering

Silicon-based anodes represent a highly promising alternative for next-generation lithium-ion batteries due to their exceptionally high theoretical specific capacity. This technology holds a strong potential to drastically increase cell-level energy density, making it a critical driver for demanding applications like electric aviation. However, commercial implementation is heavily hindered by severe structural degradation, including pulverization and mud-cracking, caused by an extreme volumetric expansion of up to 300% during cycling. To address this challenge, this thesis introduces a dual-stage processing strategy utilizing a 70/30 partial ball-milling split, where 70% of the multi-walled carbon nanotubes are ball-milled with silicon to secure local electrical contact and the remaining 30% are introduced during slurry mixing to retain long-range matrix connectivity. Morphological and electrochemical evaluations confirm that this optimized architecture successfully mitigates localized active material isolation while buffering immense physical stresses. Ultimately, the partially milled anode delivered an impressive initial

discharge capacity of approximately 2,300 mAh g^{-1} and maintained stable high-capacity retention, demonstrating a robust pathway toward viable, high-energy-density batteries.

TABLE OF CONTENTS

LIST OF FIGURES

LIST OF TABLES

1. INTRODUCTION AND BACKGROUND

Batteries have been one of the fundamental components of electrical devices since the invention of the Voltaic pile by Alessandro Volta in 1800. [1] They provided the first practical source of continuous energy which enabled the future innovations throughout the industrial revolution. By the late 1970s to 2000s, Sir Michael Stanley Whittingham, John Bannister Goodenough, and Akira Yoshino explored the new idea of battery that is rechargeable with the new lithium-ion battery (LIB). [2, 3] The best LIB chemistry, nickel cobalt manganese (NMC), has the theoretical and practical limit of 900 and 700 W h kg^{-1} recorded in 2023, respectively. [4, 5] Despite its significant increase in energy density relative to the first generation of rechargeable battery using lead acid chemistry, many technologies were being held back by four main areas: technical limitations, safety risks of thermal runaway, environmental and ethical concerns, and economics of supply chain issues.

Many electric vehicles have superior driving performance, great acceleration and zero emissions. [6] However, its real-world practicality suffers significantly from technical limitations. LIBs are heavy and massive. Compared to gasoline, they can't store that much of the energy per unit weight and volume. [7] Hence, EVs require bulky battery packs, often 15-35% of the vehicle's gross weight, to achieve a comparable range to the internal combustion engine cars. [8–10] The second drawback is the risk of fire from thermal runaway, which can occur if the battery is punctured, overcharged, overheated, or pierced by dendrite growth. [11] Ethical mining, ecological impact, and complexity of recycling of batteries are in heavy debate that often linked to human rights and ecosystems in the communities. [12–14] Lastly, most of the raw materials and manufacturing capacity are concentrated in a few countries, which creates geopolitical risks and price volatility. [15]

The development of the new battery chemistry using novel advanced materials that can improve not only the energy density, solving technical limitations, but also safety, longevity, and cost will benefit multiple communities around the world in variety of applications, from grid energy storage to the small robot medical devices.

2. LITERATURE REVIEW

The Industrial Revolutions – beginning with the steam engine in the 1760s and the internal combustion engine in the early 1900s – fundamentally transformed daily life [16] These eras have shifted societies from manual handcrafts to mechanized factory production, fueling economic growth, technological innovation, and urbanization. As industry evolved from stationary machinery to portable applications, the development of the battery became essential, providing a stable and mobile power source. [17]

Voltaic pile, the world's first battery, made from zinc, copper electrode discs, and paper soaked with salt water as an electrolyte, was assembled in many layers to reach the desired voltage. However, there are many flaws in the design where there was hydrogen gas accumulation at the cathode, causing current limit cell polarization and shorts due to electrolyte contamination. [18, 19] The next iteration in the battery development timeline is the invention of lead-acid battery by a French physicist Gaston Planté, the first rechargeable battery. (**Figure 1(a)**) Combining two lead sheets, one lead anode and a lead oxide cathode, separated with rubber strips and submerged in the sulfuric acid, this makes the lead-acid battery one of the first mainstream batteries which remains the most widely used rechargeable battery in the world today, illustrated in **Figure 1(b)**. [20] Nonetheless, the bulkiness, low energy density, and liquid electrolyte are impractical for many mobile applications. The alkaline battery developed in 1949 by a Canadian chemical engineer, where a manganese oxide cathode, a powdered zinc anode, and an alkaline electrolyte are used, successfully replaced zinc-carbon battery which was the first modern small battery for the masses. [21] However, it still faces significant shortcomings, including the tendency to leak from the alkaline electrolyte, high internal resistance, and sloping discharge curve which drastically impact its performance and its non-rechargeable property makes it less practical. [22] The next rechargeable battery, Nickel Metal Hydride (NiMH), shown in **Figure 1(c)**, was developed in the late 1980s by Research Center Battelle-Geneva as a direct response to the environmental and limitation of Nickel-Cadmium (NiCd) battery, which has been the standard rechargeable battery since the 1940s. [23] As it has less environmental impact and double the energy density than its predecessor, NiMH still remains a massive presence in the industry 80 years later.

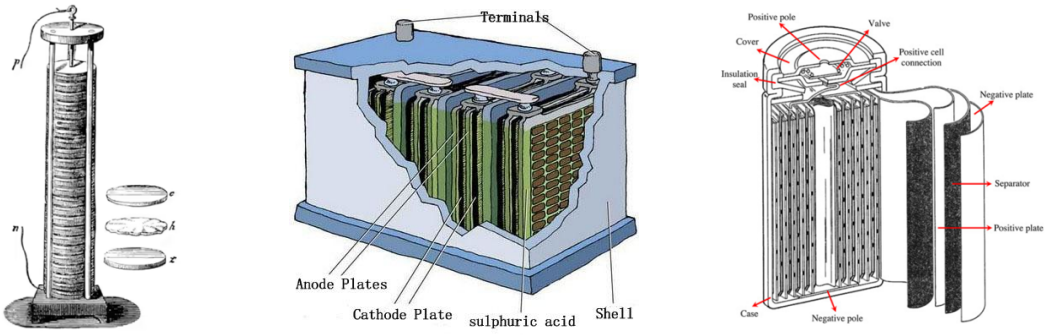

(a) (b) (c)

Figure 1 | The schematic of (a) Voltaic pile, (b) lead-acid battery, and (c) alkaline battery. [24–26]

The development of lithium-ion battery was driven by global necessity during the oil crisis of the 1970s, limitations of existing technology, and scientific curiosity. [25] The oil shortages and elevated fuel prices forced us to look for alternatives to fossil fuel. One of the solutions is to store electrical energy in the battery, aiming to create a fossil-fuel free society. An English Chemist, Sir Michael Stanley Whittingham, invented the first rechargeable lithium-ion battery (LIB) using lithium metal as an anode and disulfide (TiS_2) as a cathode, which is called lithium titanium disulfide (LTS) battery. [26] The efficiency of lithium-based batteries is heavily dependent on host materials ability to undergo reversible intercalation. As shown in **Figure 2(a)**, hexagonal titanium disulfide (h-TiS_2) serves as a model layered transition metal dichalcogenide. [27] The structure consists of TiS_2 octahedral linked in sheets which held by weak van der Waals forces. These gaps provide a pathway for lithium ions (Li^+) to insert themselves into the lattice. Specifically, lithium can occupy two distinct types of interstitial sites: octahedral sites (I), which is more energetically favorable, and tetrahedral sites (II), which may be occupied depending on the lithium concentration and the diffusion pathway. The practical application of this material is shown in **Figure 2(b)**, in the electrochemical cell diagram. [28] During the discharge process, the anode undergoes oxidation, releasing Li^+ into the electrolyte. These ions migrate across the barrier/separator into the TiS_2 cathode. The process is highly reversible as called charging, allowing the cathode material to slightly expand and contract. Nevertheless, the lithium metal in the LTS battery undergoes a severe dendrite formation at the surface after multiple charge-discharge cycles, as shown in **Figure 3**. The uncontrolled growth of metallic lithium dendrites from the anode penetrates the separator which can create a direct path to the cathode, leading to internal short-circuiting and potential thermal runaway, and is the main reason why many commercial batteries use graphite as a substitute.

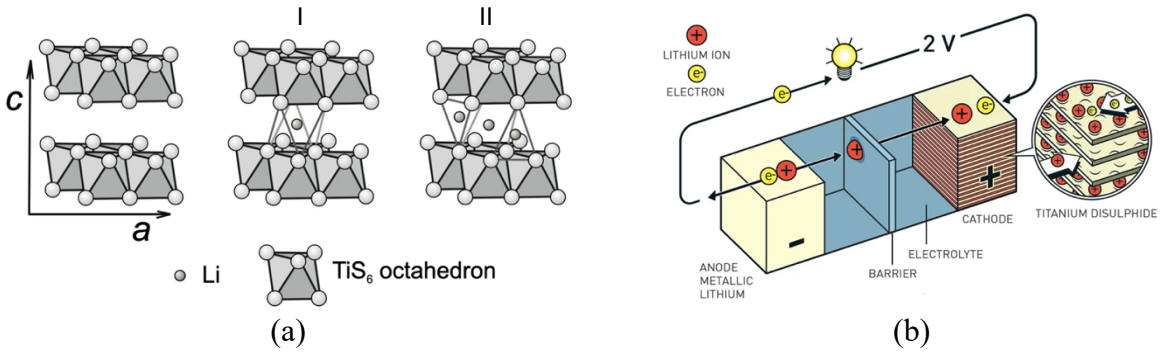

Figure 2 | TiS_2 structure and electrochemical cell. (a) Models showing lithium-ion filling in octahedral (I) and tetrahedral (II) positions of h-TiS_2 lattice. (b) Operational diagram of a lithium/titanium disulfide battery featuring a metallic lithium anode and Li_xTiS_2 cathode.

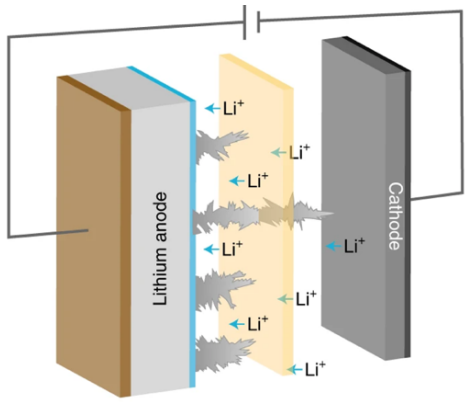

Figure 3 | Schematic of lithium dendrite formation.

The second breakthrough was an invention of a powerful LIB using cobalt oxide as the cathode, which is called the lithium cobalt oxide ($LiCoO_2$ or LCO) battery, shown in **Figure 4**, by John Bannister Goodenough. [29] It offers high operation voltage, similar specific capacity as LTS battery, and is ideal to use in consumer electronic applications, where the potentials are cost-effective, nontoxic, and environmentally friendly while giving a stable charge-discharge voltage. [30] This cell offers 4-5 V potential and a diffusion coefficient of 5×10^{-9} cm^2 s^{-1} at room temperature, using $LiBF_4$ in propylene carbonate as an electrolyte and lithium metal or $Li_{0.1}V_2O_5$ as counter/reference electrodes. However, the design's bottleneck shifted to the anode, needing higher potential and leading to a search for suitable carbon materials. Despite high energy density, these batteries suffer from thermal instability and limited cycle life.

Simultaneously, Akira Yohino and his research group identified that petroleum coke was stable under electrochemical conditions. [31] The illustrations in **Figure 5** shows the combination of LCO and petroleum coke anode, resulting in the charging voltage of 4.1 V with a recorded energy density of 80 W h kg^{-1}. This technology significantly improves the safety of the battery when experiencing external and internal damages.

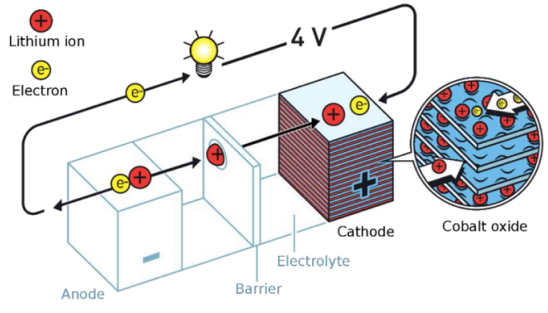

Figure 4 | Lithium-based battery using Li_xCoO_2 as cathode. [32]

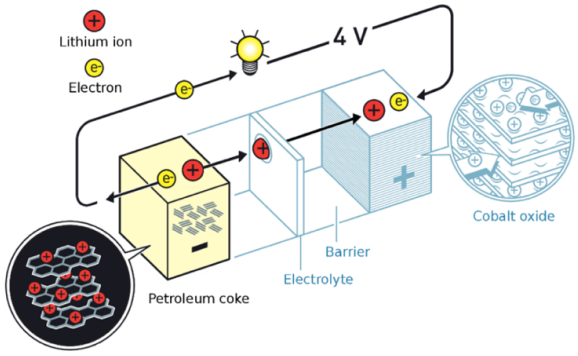

Figure 5 | Schematic of lithium-ion battery using petroleum coke as anode material. [33]

Another research found out that graphite has a great potential of being an anode material combined with an appropriate electrolyte composition. This causes a formation of solid electrolyte interphase (SEI) at the graphite electrode during charge/discharge cycle, protecting the carbon material from exfoliation and decomposition. Ther performance of the battery can get up to 200 W h kg^{-1} with 4.2 V of charging voltages. The LCO battery with graphite anode mostly utilized in today's commercial electronics, e.g., smart phones, wearables, laptops, and small electronic devices.

John Bannister Goodenough found another breakthrough in a new cathode material for LIB which is lithium iron phosphate ($LiFePO_4$, LFP) in the late 1990s. Unlike LTS and LCO, the LFP has the structure belongs to olivine family which has good structural reversibility. Illustrations in **Figure 6** shows a similarity between $LiFePO_4$ and $FePO_4$ isostructural, respectively, with heterosite during charge/discharge cycles. This helps reduce battery degradation while improve battery capacity with faster charging/discharging and long-lasting performance. Nowadays, the LFP battery are used in application that requires high power, for example, power tools, short to medium range EVs, and grid storage.

To further increase the capacity of LIB, the development of new battery composition using nickel, cobalt, and manganese has been researched called lithium-nickel-manganese-cobalt oxide ($LiNi_xMn_yCo_zO_2$, NMC). [34] The NMC111/333 electrode using $LiNi_{0.33}Mn_{0.33}Co_{0.33}O_2$ composition, can deliver initial discharge capacity greater than 300 mA h g^{-1} at 0.5 mA/cm^2 and the structure is shown in **Figure 7**. Ni-rich NMC variants like NMC622 ($LiNi_{0.6}Mn_{0.2}Co_{0.2}O_2$) and NMC811 ($LiNi_{0.8}Mn_{0.1}Co_{0.1}O_2$) were developed for higher specific capacity. [35, 36] These batteries are used in high-performance electric vehicles due to their lighter weight compared to LFP batteries.

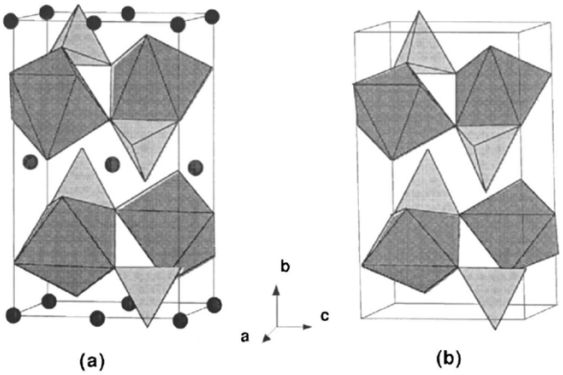

Figure 6 | Crystal structure schematic of (a) $LiFePO_4$ and (b) $FePO_4$.

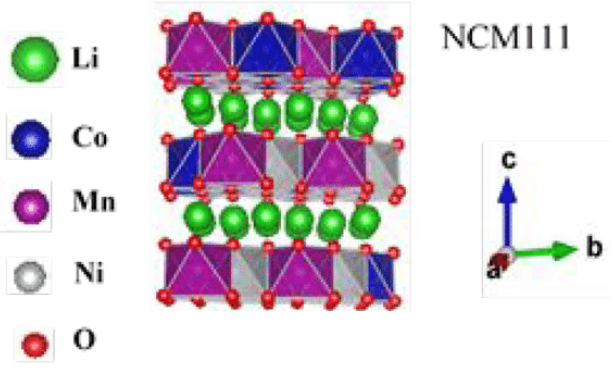

Figure 7 | Crystal structure of NMC111. [37]

While nickel-rich NMC cathodes in LIBs offer high specific capacity and superior energy density, they suffer from several significant shortcomings primarily related to premature degradation and structural instability. [38] The mechanical degradation of the crystal structure is one of the factors that promote capacity fading and impedance growth over time. The layered rhombohedral structure reconstructed into a disordered spinel ad ion-insulating cubic rock-salt phase which increases interfacial resistance and inhibits Li^+ insertion and desertion. Repetition of charge-discharge cycle causes anisotropic expansion and contraction of the lattice, generating microstrains leading to microcracks, weakening particle connections and parasitic reactions. Nickel-rich materials tend to release oxygen from the lattice at high voltages or temperatures. This released oxygen can react with electrolyte, contributing to gas evolution and premature decomposition of electrolytes. The oxidation of electrolyte with Ni^+ can also causes corrosion, resulting in the thickening of cathode-electrolyte interface (CEI) and generates CO and CO_2 gases.

3. RESEARCH QUESTIONS AND OBJECTIVES

The current plateau in battery energy density is largely defined by the theoretical chemical limitations of the cathode at approximately < 250 mA h g^{-1}. [39] Practically, the utilization is limited to 200 mA h g^{-1} in the laboratory environment. [40] In order to push the capacity, the concentration of nickel needs to be very high, thus destabilizing the crystal structure and increasing the risk of thermal runaway. Consequently, further development of NMC has surpassed the point of diminishing returns, where massive research efforts result in only tiny gains in capacity.

On the other hand, anode side of the battery offers a much higher headroom for improvement. [41] For many decades, battery has been using graphite as the anode where the theoretical limit of 372 mA h $g^{-1}$and it has been fully utilized by many iterations. [42] By changing the materials of the anode could potentially create a significant paradigm shift in the battery industry. One of the candidates is silicon, for instance, exhibits a theoretical capacity of approximately 3,600 mA h g^{-1}, nearly tenfold of the current graphite. [43] This massive difference saw the potential of the next-generation battery from these new materials, allowing an instant 30-50% improvements in total cell energy density.

Silicon, an element number 14 in the periodic table, is the second most abundant element on Earth. The integration of silicon mitigates dependence on specific geographic regions for high-grade graphite, promoting localized production and enhanced sustainability. [44] With superior theoretical capacity, Si anode also shows intermediate working potential with lithium and lithium-ion at ~0.5 V, in compare with graphite anodes at ~0.05 V, causes the mitigation in safety concerns of deposition of lithium during cell overcharge. It also offers faster Li+ kinetics during charging and discharging, lower energetic barrier for Li+ inside the bulk of materials, allowing extreme fast charging (XFC) than graphite. [43] Furthermore, the benefit of fast-charging silicon permits higher redox potential than that of graphite which is less subject to lithium plating during charging process, which would severely degrade the cyclability and safety. [45] The XFC will allow 0-80% charge time under 15 minutes, which is very comparable to traditional filling time at the gas station in the ICE vehicles. [46] Graphite anodes also heavily struggle in low temperature environment due to slow kinetics of charge transfer and slow diffusion. [47] These are why silicon has been raised as the premier candidate for next-generation anodes, and it will be the main subject of this thesis.

Despite all the advantages of silicon anode, as of 2026, it is still not the industry standard for the next-generation battery with some key technical challenges. The first primary obstacle is its extreme volumetric expansion during lithiation (charging) and delithiation (discharging) by approximately 300%. [48] This cyclic mechanical stress causes the silicon to pulverize, severing and hindering the flow of Li^+ within the cells, shown in **Figure 8(a)**.

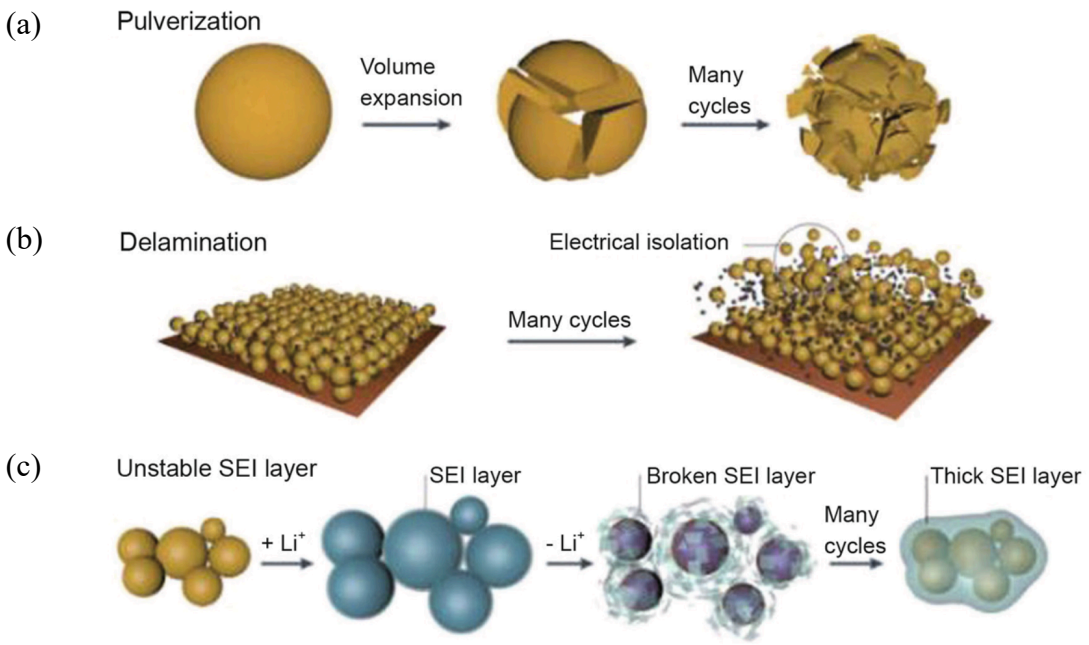

Figure 8 | Schematic diagrams of key challenges of silicon anodes from (a) pulverization, (b) delamination, and (c) unstable SEI layer. [49]

Another failure point is delamination of the silicon layer from the current collector substrate, illustrated in **Figure 8(b)**. [50] As long as the Si film remains a good contact with the current collector, despite its fracture or microcracks on the film, the active material will remain electrochemical active. The delamination severely impacts the capacity of anode, reliability, and performance of the overall cells. The last shortcomings of the silicon anode is the unstable SEI layer from multiple charge-discharge cycles. [51] A rupture in the SEI layer, shown in **Figure 8(c)**, causes unexpected continuous side reactions with the electrolyte, resulting in the formation of thick SEI layer with a high impedance. Hence, the capacity rapidly and prematurely faded due to loss of initial active materials.

The objective of this thesis is to advance the development of next-generation silicon-based anode system that overcome the inherent limitations constraining current lithium-ion technologies. This work focuses on investigating advanced nanostructured silicon architectures and composite material integrations capable of mitigating expansion-induced failure. Through these approaches, the thesis aims to establish a silicon anode framework that not only exceeds the performance of current state-of-the-art NMC batteries but also satisfies the electrochemical stability, safety, and long-lasting requirements for next-generation high-energy battery applications.

4. APPROACHES

4.1 Material Selection

4.1.1 Rationale for Active Material Selection

The electrochemical behavior of LIB electrode materials is often in lithium half-cell configuration, where the electrode is in the cell with a lithium metal as a counter and reference electrode. Unlike the full-cell configuration where cathode and anode resemble to the final battery, the half-cell testing allows researchers to comprehend electrode performance with a lithium metal cathode as the reference, identifying properties, performance metrices, and potential issues. The reason why the lithium metal is used due to its large specific capacity of 3,860 mA h g^{-1}, allowing sufficient capacity to test the engineered electrode without any bottlenecking at the counter electrode and can maintain a constant 0 V between Li/Li^+ potential. [52]

Silicon is an abundant element that offers major advantages over graphite as an anode material, including much higher theoretical capacity and a safer intermediate operating potential. Faster Li^+ diffusion nature of the silicon and lower diffusion barrier allow the battery to quickly charge, while operating at a higher redox potential, which reduces the risk of lithium plating during charging. Silicon anode also performs better than the conventional graphite anode, where it doesn't limit its performance at low-temperature conditions.

In this work, silicon nanoparticle (n-Si) is used as a base slurry composition. [53] Instead of using larger silicon particles that suffers from pulverization, the n-Si can better mitigate extreme volume expansion. The structure of n-Si also avoids cracking and fragmentation at ~150 nm, preventing breakdown of the electrode material. The smaller size allows shorter diffusion paths for lithium ions, further enhancing the kinetics throughout the cells, and the benefit of larger surface area promotes good contact with the overall matrix, preventing capacity loss during inactivity.

4.1.2 Conductive Additives and Binder Systems

Carbon Nanotubes (CNTs) are cylindrical quasi-one-dimensional (1D) nanostructures composed of multiple rolled-up graphene sheets, specifically multi-walled carbon nanotubes (MWCNTs). [54] These carbon network materials have superior mechanical and electronic properties that are beneficial for the battery as a good conductive network, unlike its single-walled counterparts, which faces higher production cost, harder to fabricate, and scale the production. [55–57] The MWCNTs are utilized primarily to address the massive volume expansion that silicon undergoes during lithiation. This nanoscale rebar, a reinforcing structure core, creates a flexible, interconnected frame that maintains electrical pathways even the micro cracks are present on the silicon. [58]

The utilization of Super P® (Carbon Black) further enhances the conductivity of the electrodes. Combining the Super P® with CNTs creates a hierarchical conductive network that

address the limitations of using either material alone. Small particles of the Super P® help filling the voids between the active material silicon, which can be said that the CNTs represent large highways and the Super P® as many small local roads that help guiding into broader areas. [59] Furthermore, the smaller surface area of the Super P® helps forming a more stable SEI, resulting in better initial Coulombic Efficiency. [60] Furthermore, this hybrid approach aids the formation of homogeneous slurry of conductive agents, preventing the entanglement of the CNTs.

To complement the MWCNT network, Lithium Poly (acrylic acid) or LiPAA is used as the binder. The LiPAA possesses a high concentration of carboxylate groups that form strong hydrogen and covalent bonds with silicon surface, limiting and containing electrode during expansion while providing better cycling capacity retention. [61–63] Unlike the traditional PVDF binder that forms weak van der Waals interactions, the LiPAA also gives the flexible hydrogen-bonded backbone, low swell ability, good adhesion, chemically, and mechanically stable to the oxide surface of silicon that mitigates volume changes and retaining good structural integrity. The use of PAA-based binder also improves the ICE and provides a stable SEI layers from the polyether structures. [64, 65]

4.1.3 Current Collectors

Copper is one of the best electrical conductors, second to silver. It is also a material of choice as a current collector in commercial LIBs because of its ductility, chemically stable in air, mature manufacturing process, low price, and lightweight. [66, 67] Unlike aluminum, there are unwanted reactions, also known as alloy, with lithium at low potential that heavily affect the electrochemical performance. It can withstand the mechanical expansion of silicon during lithiation while maintaining electrons flowing efficiently.

4.2 Preparation of Silicon Anode Electrode

4.2.1 Slurry Formulation

There are three main components in the slurry, namely active material, binder, and conductive additive, with a mass ratio of 6:2:2 and combined mass of 200 mg. The active material is 99% silicon with diameter of 100 nm (Skyspring Nanomaterials, USA). LiPAA binder (10 wt%) is formulated from 35 wt% liquid PAA (Sigma-Aldrich, USA) and 99.95% $LiOH \cdot H_2O$ (Sigma-Aldrich, USA) using deionized water as a solvent. Carbon black (Super P®) is used as the conductive additive for battery electrode. With the addition of CNT, the mass ratio changes to 6:2:1:1, of silicon powder, binder, conductive additive, and MWCNT, with the same combined mass of 200 mg.

4.2.2 Mixing Procedure

Active material and carbon black are combined in ceramic jar which will then be ball milled using mini-planetary milling machine (PMV1-0.4L, MSE Supplies, USA) using a specific sequence. The machine runs in forward (FWD) and reversal (REV) running mode where 30

minutes are run in each FWD and REV session. In between each session, the machine stops for 30 minutes, and the cycle is repeated for 4 times. When performing a mixture of CNT, 70% of the total MWCNT portion is added to the ceramic jar to get milled and the remaining amount will be later added during slurry formation.

Later, the milled powder will be mixed with remaining portion of binder and 600 μL deionized water solvent in planetary centrifugal mixer (ARE-310, THINKY, Japan) to form a uniform slurry for 20 minutes at 2,000 rpm.

4.2.3 Coating and Drying

9-μm-thick copper current collector (MTI, USA) is placed on a smooth glass current-collector bed that was thoroughly cleaned with ethanol to remove superficial contaminants. Thickness of the doctor blade is set to 50 μm and the slurry is spread uniformly on the current collector and automatic film coater (MSK-AFA-II-VC, MTI, USA) is used to ensure a continuous coat with traverse speed of 5 mm s^{-1}. The film was first dried at 60 ºC for one hour and then at 80 ºC overnight before being punched out, all under vacuum in a vacuum oven (DZF-6050, Intertek, UK).

4.2.4 Electrode Punching

The electrode was punched out into disk of 13 mm in diameter (mass of active material is ≈ 0.5 mg cm^{-2}) using a handheld electrode cutter (CAN-7-10-13, Beyond Battery, Singapore). All the test electrodes were stored in glovebox (VTI, USA) where H_2O and O_2 concentration are under 0.01 ppm in an argon environment to prevent oxide and nitride formation.

4.3 Preparation of Lithium Electrode

Counter electrodes were prepared by using lithium foil with the thickness of 0.75 mm (MTI, USA) and punched out into disks with diameter of 15 mm. The lithium disks were all processed in the argon-filled glovebox to avoid any contamination, oxidation and corrosion when exposed to outside air. Both surfaces on both sides were scraped using plastic spatula (LevGo, USA) in the glovebox to remove surface passivation films, like oxide, nitride and carbonate layers.

4.4 Electrolyte Preparation

4.4.1 Electrolyte Chemistry Selection

Electrolyte utilizes a ternary solvent blend of Ethylene Carbonate (EC), Ethyl Methyl Carbonate (EMC), and Dimethyl Carbonate (DMC) in a 1:1:1 volume ratio, which balances high ionic conductivity and low viscosity with the necessary dielectric constant for salt dissociation. The primary salt is LiPF6, while the critical additives are Fluoroethylene Carbonate (FEC) and Vinylene Carbonate (VC). This specific formulation is engineered for Si compatibility by addressing volumetric expansion during lithiation.; FEC and VC are sacrificial agents that decompose at a higher potential than the base solvents to form a more robust, flexible, and cohesive

SEI. [68] These materials are better at withstanding mechanical stress compared to the standard carbonate interfaces, effectively suppressing continuous electrolyte consumption.

4.4.2 Preparation Procedure

To synthesize the electrolyte, 0.912 g of lithium hexafluorophosphate ($LiPF_6$) was combined with 2 mL of each solvent: EC, EMC, and DMC. Subsequently, 6.9 g of 5% FEC and 0.07 g of VC additives were incorporated into the mixture. All procedures were conducted within an argon-filled glovebox, ensuring an environment with < 0.01 ppm of water vapor and oxygen.

4.5 Separator Selection and Preparation

Tri layer polypropylene/polyethylene/polypropylene (PP/PE/PP) separator (Celgard® 2325, Celgard, USA) was used as a separator. This Tri layer allows the battery to have a built-in shutdown mechanism as the temperature of the cell increases. The PE core, which has a lower melting point at ~130 ºC, will melt and close the pores in the separator porous structure to stop the ion flows, while the shell remains intact to prevent any short circuit. [69] It also offers good balance of ionic conductivity, medium porosity that provides good energy performance with low self-discharge, chemical, and thermal stability. [70] The separators were cut into 19 mm disk and dried in the vacuum oven at 60 ºC overnight prior the cell assembly. The remaining ones were stored in an argon-filled glovebox.

4.6 Coin Cell Components and Casing

4.6.1 Hardware Description

2032-type coin cells were assembled that made from SS316L. Two SS316L spacers, one with 0.5 mm- and 1 mm-thick, were used to fulfill remaining gap. To make sure a uniform contact, 1 mm-thick SS316L wave spring was used to maintain constant axial pressure.

4.7 Cell Assembly Process

4.7.1 Layer-by-Layer Assembly

The cells were assembled in the Ar-filled glovebox with controlled H_2O and O_2 content to be < 0.01 ppm. The sequence starts from the negative cover of the coin cell, then a spring was placed followed by two spacers. Polished lithium metal disk was placed on top of the spacers and 30 μL of electrolyte. A spacer is carefully placed in the center of the cell, followed by another set of electrolytes, then the silicon anode where the active material was facing down toward the lithium disk. Lastly, the positive cover of the coin cell was placed on the very top. Note that the cells can also be assembled in reverse, starting from the positive cover at the bottom.

4.7.2 Crimping Conditions

The battery cells were pressed on using hydraulic crimper (MSK-110-S, MTI, USA) with the crimping pressure of 50-80 kg cm^{-2} and it is certified for use inside the glovebox. The pressure

was released momentary after the pressure reached the target crimping pressure to ensure a good seal and allows the internal stresses to stabilize.

4.8 Electrochemical Testing Procedures

To evaluate the electrochemical viability of the cell chemistries, a comprehensive testing protocol was implemented using Arbin Battery Test Machines (LBT21084UC, Arbin Instruments, USA). The evaluation was structured to transition from initial surface stabilization to high-drain kinetic analysis and accelerated aging studies.

4.8.1 Formation Cycling

Formation cycling was initiated to facilitate the controlled growth of the SEI on the anode to prevent any irreversible consumption of electrolyte and lithium ions. [71] This occurs during the initial charge and discharge cycles, where the electrolyte undergoes a localized decomposition to form a stable protective film, allowing the inner structure to stabilize after the material undergo mechanical expansion and contraction for the first time. C-rate during this formation cycle was capped at 0.1C.

4.8.2 Rate Performance Tests

Characterization through various C-rate serves as a rigorous diagnostic tool to evaluate the kinetic polarization and mass transportation efficiency. By subjecting the cell to a progressive range of current densities, from 0.1C to 5C, can identify any performance bottleneck in the cell or electrode architecture. At lower rate, 0.1C or 0.33C, the cell typically expresses its maximum capacity due to longer discharge rate, allowing sufficient time that lithium ions can properly diffuse through the active materials. As the rate escalades toward 2C or 5C, the internal resistance becomes higher, causing voltage hysteresis and heat generation. By comparing the analysis data, identification of deleterious phenomena, for example, lithium plating when charging rate is over the intercalation kinetics of the anode, diffusion limitations of electrolyte and thermal degradation that affect the breakdown of SEI layer.

4.8.3 Long-Term Cycling

The long-term electrochemical stability of cells was evaluated through a cycling protocol of 1,000 charge-discharge cycles conducted at a constant rate of 0.1C. To ensure a comprehensive assessment, a potential window was established between a lower cut-off voltage of 0.1V and an upper cut-off voltage of 1.5V. While specific thermal safety limits were not manually figured, the system operates under the default configuration to automatically terminate the test when an abnormally is detected. This extensive testing serves to characterize the capacity retention and Coulombic efficiency of the cell over a long operation lifespan, providing data on the evolution of SEI layers and long-term chemical stability and reversibility.

4.9 Post-Cycling Characterization

To investigate the morphological evolution and degradation mechanisms of the silicon anodes, the cycled coin cells were carefully disassembled after reaching their designated cycle life. This process was conducted in an argon-filled glovebox to maintain a moisture-free and inert environment. The electrode was rinsed with DMC to remove any residual salts and prevent the formation of salt-based artifacts on the electrode surface during drying. To remove the residual DMC solvent, the rinsed electrode was placed on the SEM stage and subjected to a vacuum drying process within the glovebox antechamber. This step is for the prevention of solvent evaporating during imaging. Once dried, the stage was sealed inside an inert-atmosphere transfer vessel before being removed from the glovebox, preventing the formation of any oxide layers on the surface that would compromise the accuracy of the top- and cross-sectional-view SEM.

5. RESULTS AND DISCUSSIONS

The primary objective of this study is to evaluate the performance and structural stability of silicon-based anode materials designed for high-energy density aviation applications. To bridge the gap between materials designed material synthesis and practical battery requirements, this section presents a comprehensive analysis of the experiment data. By correlating physical morphology from electron microscopy with electrochemical performance metrices – including cycling stability, rate capacity, and differential capacity.

5.1 Structural and Morphological Characterization

The surface and cross-sectional morphology of pure silicon-based anodes by standard slurry mixing protocol, denoted as Si, were first characterized to establish a performance baseline. **Figure 9(a)** indicates the electrode surface at low magnification (1,000x) after the drying process. A prominent "mud-cracking" pattern is visible across the surface. This phenomenon is typical for pure silicon active material highly contains stress accumulation from the lack of solvent surface tension that just evaporated and reinforcing conductive network. Higher magnification analysis, shown in **Figure 9(b)** reveals the particulate nature of the active material. The silicon nanoparticle appears loosely packed with significant interstitial void spaces. When the battery undergoes a lithiation process, the characteristic 300% volumetric expansion will likely disconnect electrical contact with the surrounding matrix, causing rapid capacity fade and electrode failure. Furthermore, a cross-sectional view, illustrated in **Figure 9(c)**, gives an idea on how the active material deposited on the copper current collector. While the coating is approximately 8–10 μm, the top surface appears irregular and fuzzy, further indicating a lack of structural cohesion that addition of CNTs aims to resolve.

To mitigate the structural degradation observed in pure silicon, CNTs were deployed as a conductive material and structural reinforcement, which is symbolized as SiCNT. However, standard mechanical mixing proved insufficient for achieving a homogeneous composite. Figure 10(a) indicates that while the addition of CNTs marginally reduces the severity of the macro-cracks throughout the network compared to pure Si anode. The primary cause for this limited improvement is revealed at higher magnification where the nanotubes form dense, entangled nests rather than an evenly distributed network. Since the CNTs possess a high aspect ratio and strong van der Waals forces, they naturally agglomerate. Furthermore, in the direct mixing, this agglomeration was completely isolated, leaving majority of silicon particles to bundle, like in the pure silicon, without any mechanical tethering. The cross-sectional analysis in Figure 10(b) further confirms this inhomogeneous distribution. Large, bright clusters are clearly visible, representing localized concentration of CNTs, suggesting the electrode will undergo high internal resistance and localized overpotential, as the electron transport is limited by the lack of continuous path. These observations justify the transition to high-energy ball-milling to physically de-bundle the CNTs.

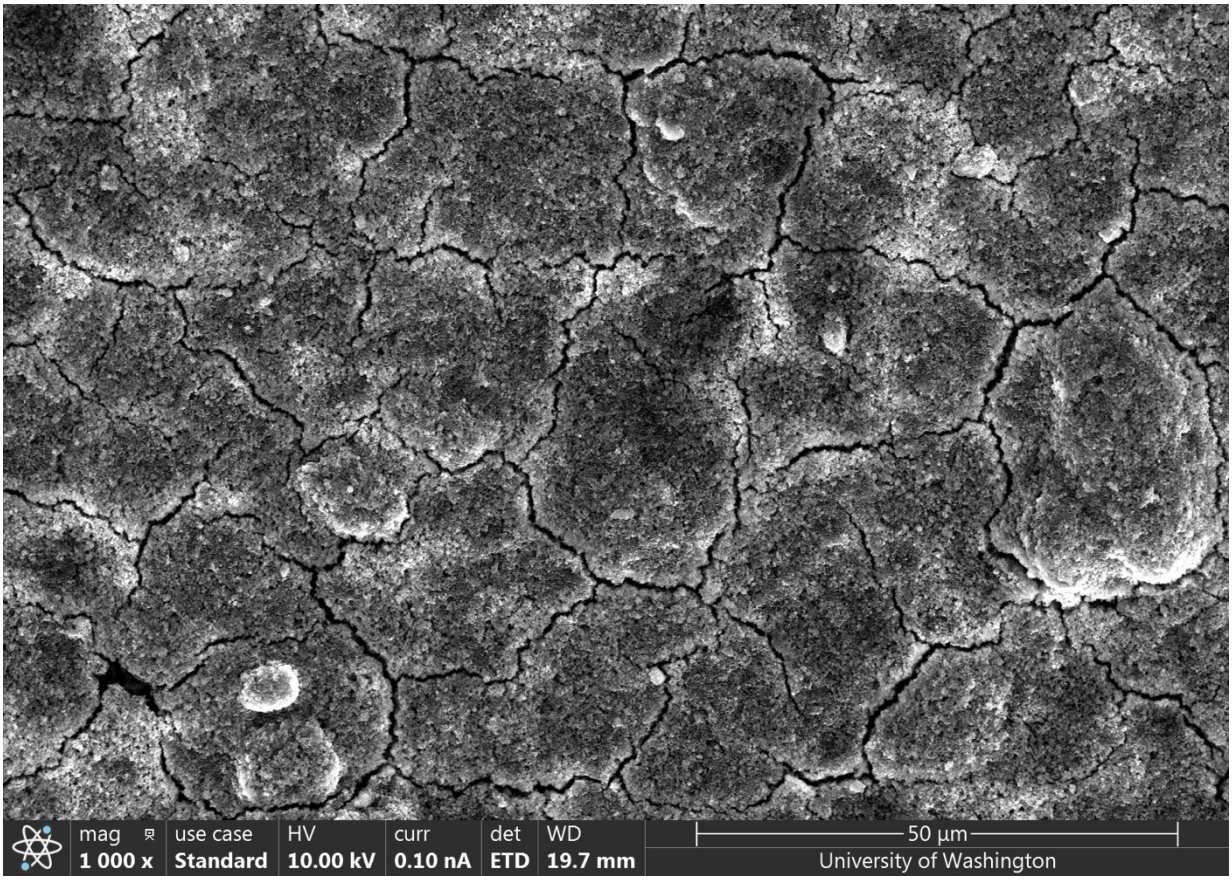

(a)

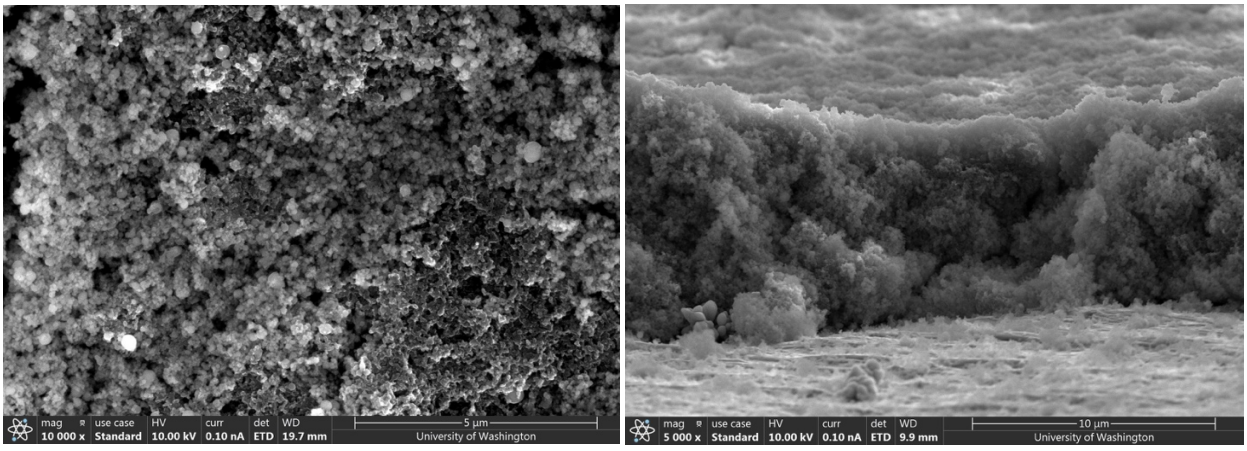

(b) (c)

Figure 9 | Scanning electron microscopy (SEM) image of a silicon-based anode surface showing (a) mud-cracking effect of the electrode, (b) agglomeration of nano-Si, and (c) electrode thickness and interface with the current collector.

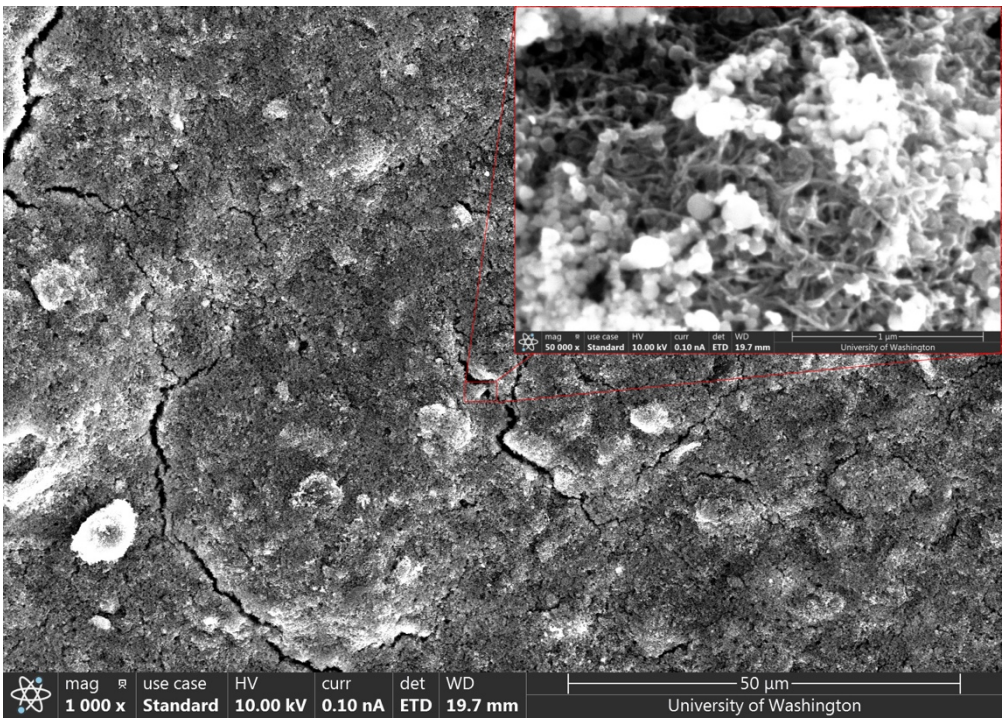

(a)

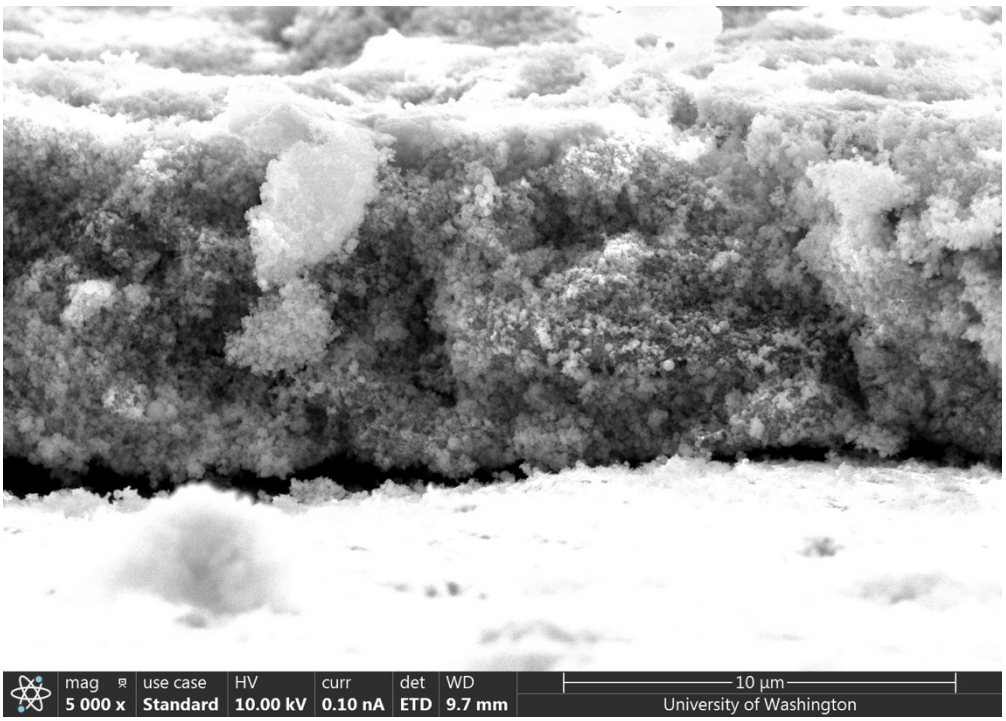

(b)

Figure 10 | SEM micrographs of the SiCNT anode prepared via direct mixing at (a) 1,000x magnification with 50,000x inset and (b) cross-section layer.

To overcome the entanglement of CNTs observed in the direct mixing protocol, high-energy ball milling (BM) was employed. This process uses mechanical shear and impact forces to physically separate CNT bundles. As shown in **Figure 11(a)**, the macro-cracking that presented in the previous samples is eliminated at 500x magnification. It indicates that the milling process successfully homogenized the binder and conductive additives where the surface appears highly uniform and continuous. At higher magnification, the individual silicon particles are no longer loosely packed but are embedded within a dense matrix. However, a critical observation at 50,000x magnification, the CNTs, while well dispersed, appear significantly shortened. The high-energy collision during the milling process is likely fracture the structure, reducing their aspect ratio. While this ensures the localized electrical contact, the loss of long-range bridging and its good mechanical properties significantly compromises the overall mechanical toughness of the electrode. The cross-sectional view in **Figure 11(b)** further shows an extremely dense packing. While this structure is beneficial in the amount of energy density, it highly limits the amount of room for the silicon to expand and contract and restrict electrolyte wetting. This over-process morphology explains the suboptimal electrochemical performance and leads to the development of the 70/30 partial milling strategy.

To address the trade-off between CNT dispersion and mechanical length, a partial ball milling strategy was implemented. In this approach 70% of the total CNTs were subjected to high-energy ball milling to ensure intimate contact and de-bunding, while the remaining 30% were added via direct mixing to preserve their original high aspect ratio. The result morphology, shown in **Figure 12(a)**, maintains the macro-scale uniformity and crack-free surface achieved like the previous ball milling process. However, the higher magnification image in **Figure 12(b)** reveals a distinct structural advantage where the presence of long, interwoven carbon nanotube throughout the matrix. This unmilled CNTs are acting as a structural support, spanning across silicon particles and potential micro-cracks. The cross-sectional analysis in **Figure 12(c)** shows a balanced density, unlike all ball milled structure. This approach provides two key advantages: the mechanical buffer of the long-range CNT network which provides the tensile strength to accommodate volumetric expansion during lithiation and delithiation, and the allowance of efficient electron transportation throughout the structure, lowering the overall cell impedance. This optimized morphology successfully integrates the high surface contact required for the charge transfer and the robustness required for long-term cycling.

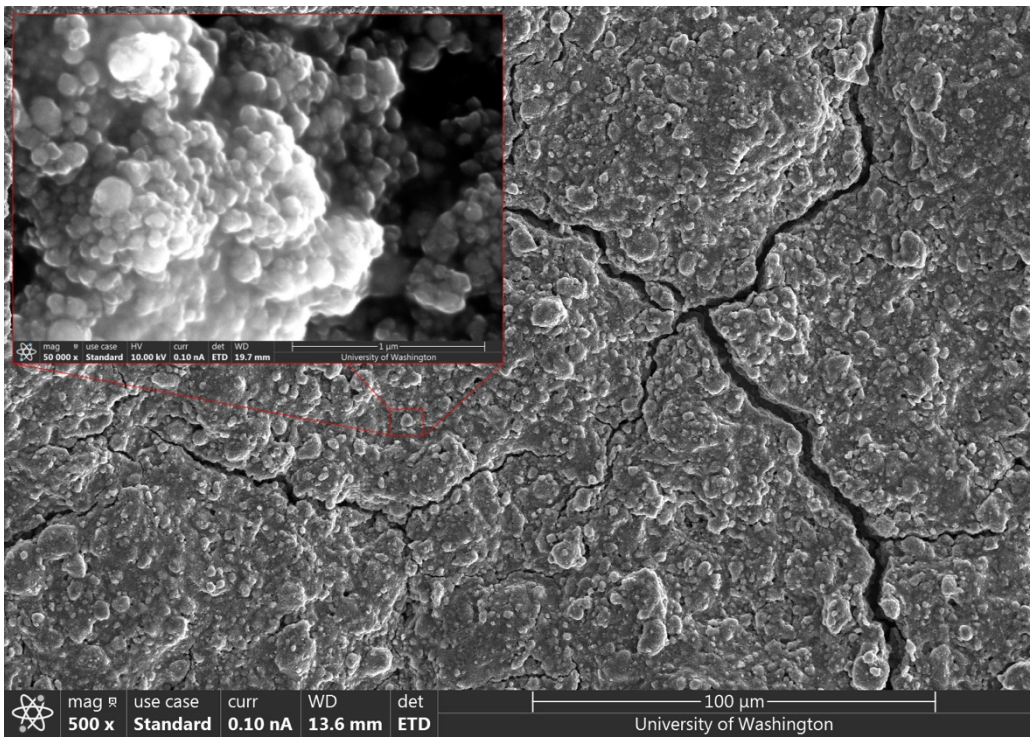

(a)

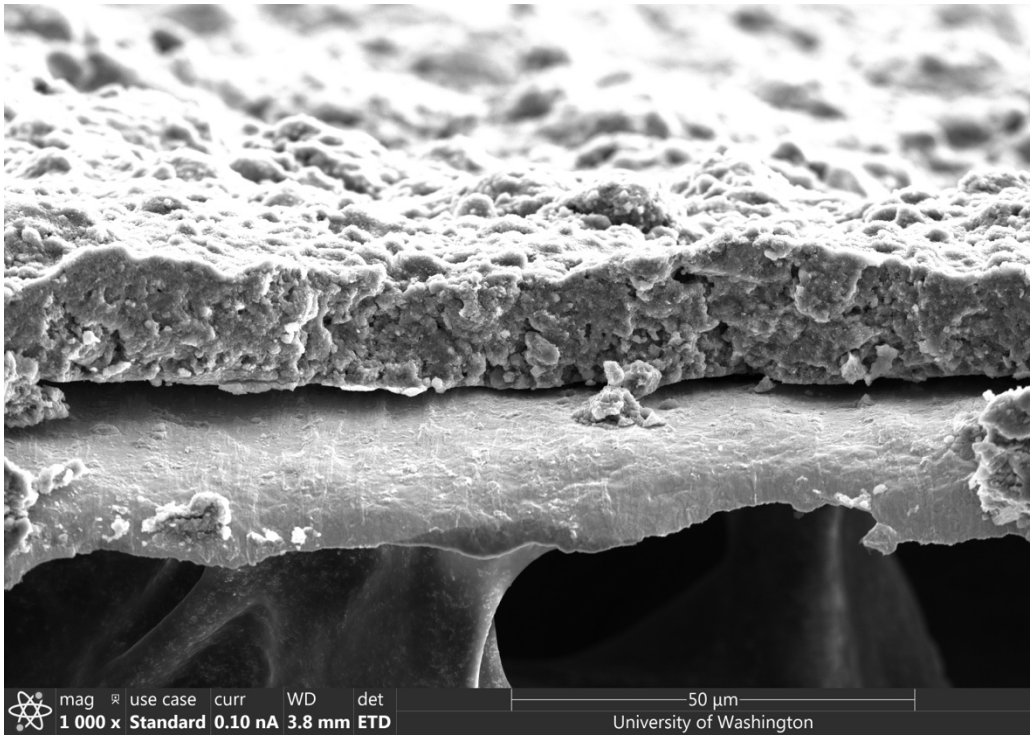

(b)

Figure 11 | SEM images of the SiCNT anode prepared using high-energy ball milling at (a) 500x magnification with 50,000x inset and (b) 1,000x cross-section layer.

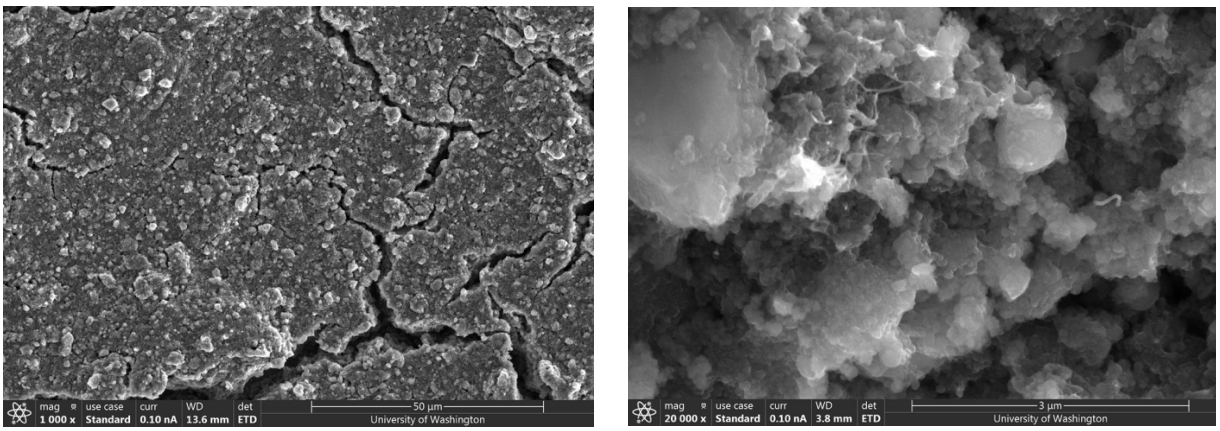

(a) (b)

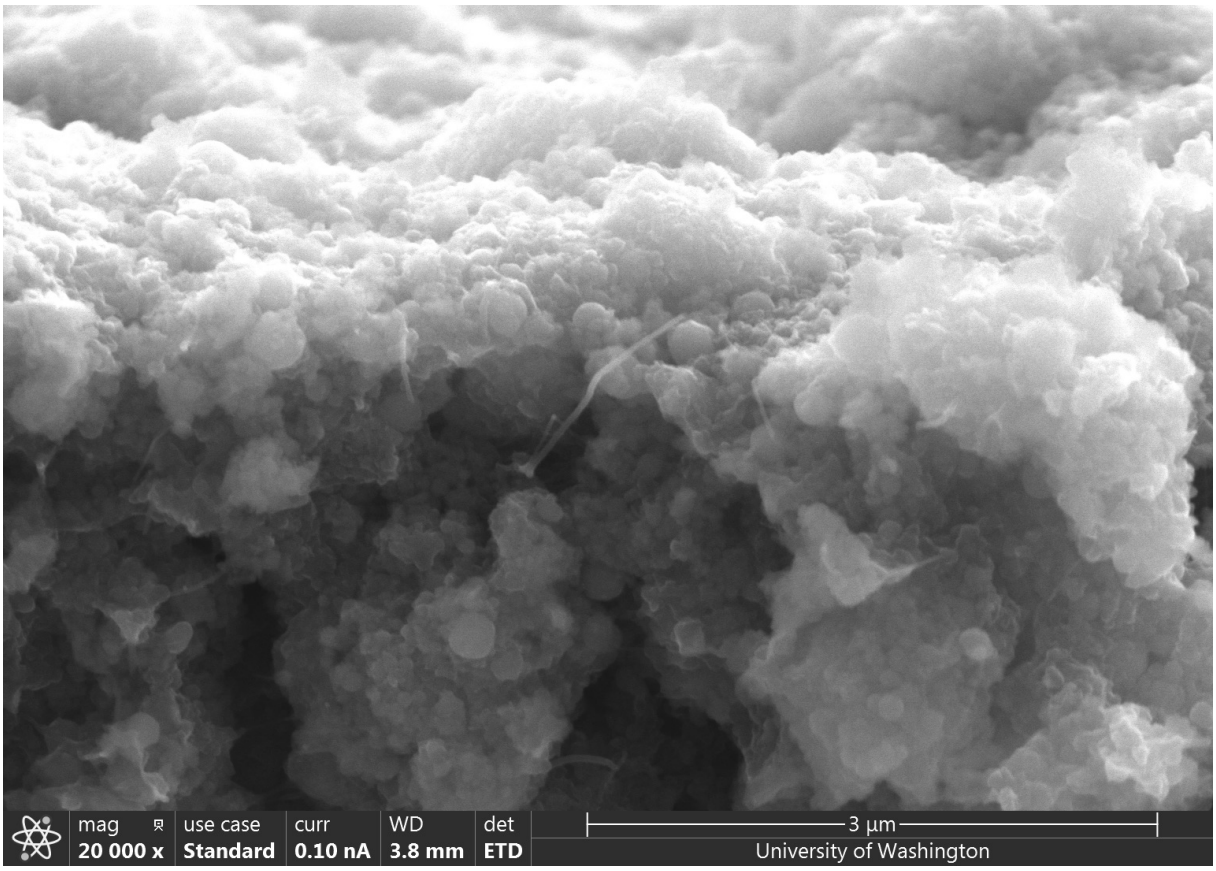

(c)

Figure 12| SEM image partially ball milled CNT in silicon anode at (a) 1,000x magnification, (b) 20,000x magnification, and (c) 20,000x magnification cross-section.

5.2 Electrochemical Signatures and Phase Transitions

The electrochemical behavior of the silicon-carbon nanotube composite, fabricated via the partial ball milling strategy, was characterized using galvanostatic cycling and differential capacity analysis. The primary objective of this section is to correlate the morphological benefits of the partial ball milling strategy structure with its electrochemical signatures and the fundamental phase transitions occurring during lithiation and delithiation.

5.2.1 Voltage Profile Analysis

As shown in **Figure 13(a)**, the material exhibits the characteristic voltage profiles associated with amorphous silicon (a-Si). During the initial lithiation, a long, sloping plateau is observed below 0.2 V, representing the conversion of crystalline silicon to amorphous Li_xSi phases or the lithiation of already amorphous regions.

The discharge curves remain remarkably consistent in shape across hundreds of cycles, although a gradual contraction in capacity is observed. This consistency suggests that the partial ball milling process creates a robust conductive network that maintains electrical contact even as the silicon particles undergo massive volume expansion. Pure silicon, shown in **Figure 13(b)**, typically show a rapid truncation of these plateaus, indicative of premature particle disconnection. Furthermore, initial and overall specific capacity of partial ball milled formula is notably higher than the pure silicon.

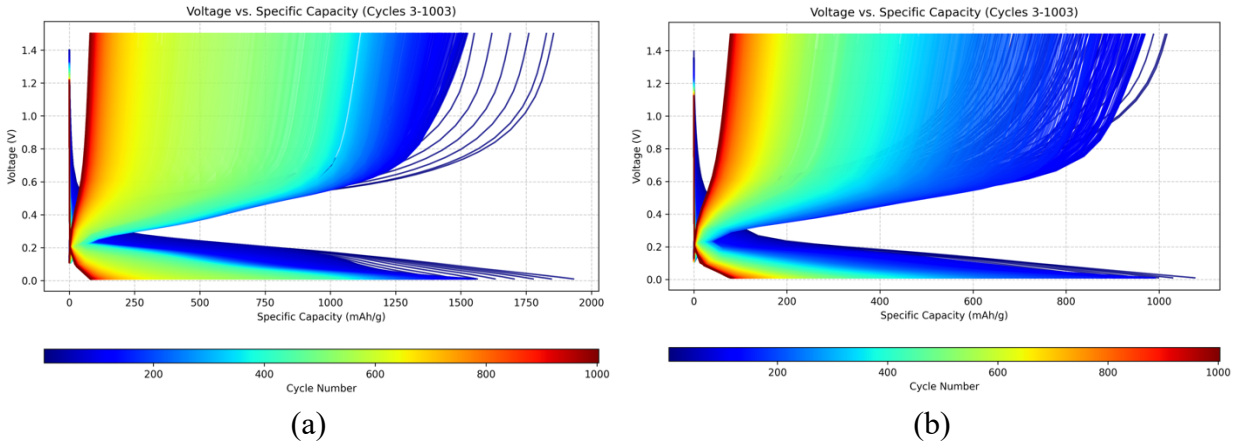

(a) (b)

Figure 13 | Voltage vs. Specific Capacity plot of (a) partial ball milling and (b) direct mixing anode at 1C, excluding the first two formation cycles.

5.2.2 Differential Capacity and Phase Transition

To further elucidate the phase transition, the differential capacity (dQ/dV) was plotted against voltage. The dQ/dV curves, shown in **Figure 14**, for the partial ball milled formula reveal distinct peaks that serve as fingerprints for the lithiation/delithiation process. Two primary peaks are visible in the cathodic region (lithiation) at approximately 0.1-0.25 V. These correspond to the sequential formation of different Li-Si alloys. In the anodic region (delithiation), another two prominent peaks appear at approximately 0.3 and 0.5 V, representing the transition from the highly lithiated $Li_{15}Si_4$ phase back to amorphous silicon. This strategy is particularly effective in preserving these signatures. While traditional high-energy ball milling can lead to excessive particle pulverization and loss of these distinct transitions over time, the partial milling approach preserved the CNT length. The web structure ensures the phase transition remain reversible and kinetically accessible.

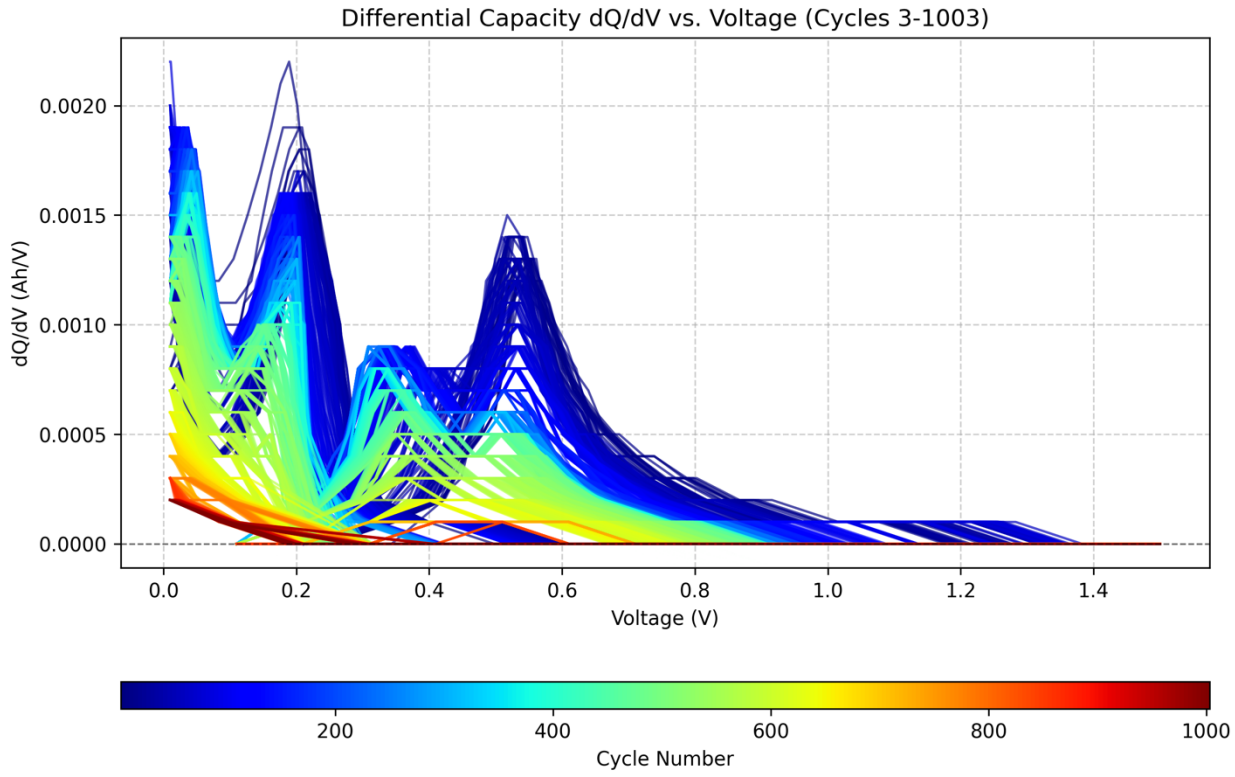

Figure 14 | Differential capacity plot of partial ball milled carbon nanotube in silicon anode, excluding the first two formation cycles.

5.2.3 Impact of Ball Milling on Structural Reversibility

The evolution of the dQ/dV peaks over hundreds of cycles demonstrates the long-term stability of the phase transitions in this composite. While there is a decrease in peak intensity, peaks do not shift significantly in voltage position. The absence of significant peak shifting (polarization) suggests that the ohmic resistance within the electrode remains relatively stable. This is a direct consequence of CNTs' where their ability to bridge cracks and maintain a continuous electron pathway, a feature that was corroborated by the SEM observations. By comparing these results of partially ball milling method to the direct mixing baseline, shown in **Figure 15(a) and (b)**, respectively, it becomes evident that the architecture of partially ball milled is essential for stabilizing the electrochemical signature of silicon during high-rate cycling.

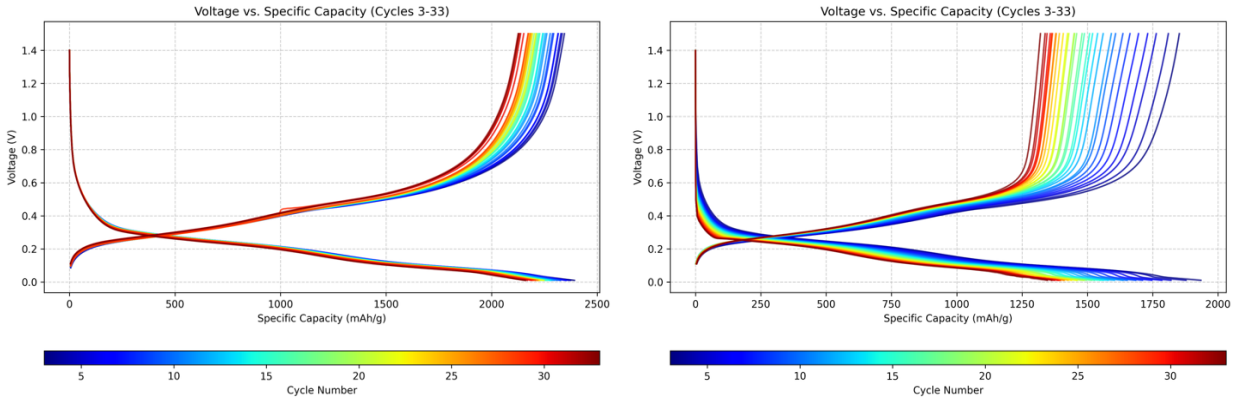

(a) (b)

Figure 15 | Voltage vs. Specific Capacity plot of (a) partial ball milling and (b) direct mixing anode at 0.1C excluding the first two formation cycles.

5.3 Influence of CNT Dispersion on Kinetic Performance

The kinetic performance of silicon-based anodes is traditionally limited by the slow charge transfer resistance and low electrical conductivity of silicon. In this section, the influence of multi-walled carbon nanotube (MWCNT) dispersion – achieved through the partial ball milling strategy – is evaluated to demonstrate how a preserved network structure affects rate capacity.

5.3.1 Comparative Rate Capability

The kinetic robustness of the electrode was evaluated using Step Mode protocols, where testing c-rate was varied from 0.1C, 0.2C, 0.33C, 0.5C, 1C, 2C, and 5C, respectively. A comparison is drawn between the optimized partial ball milled anode and the control sample prepared by full ball milling method, both shown in **Figure 16**. At low current densities, both fabrication methods can utilize the high theoretical capacity of silicon. However, as the current density is stepped up, the full ball milling shows a steep decline in capacity. This suggests that the partially ball milling process successfully distributes the CNTs to create a continuous support and conductive matrix, reducing overall potential required for electrons to transport during charging and discharging.

At the lowest current density of 0.1C, both formulations access high specific capacities exceeding 2,000 mAh/g, reflecting full utilization of the silicon active material. However, as the C-rate increases, a clear divergence emerges. The full ball milling cell exhibits a steep and progressive decline in capacity beginning at 0.33C, with near-complete capacity loss at 5C. By contrast, the partial ball milling electrode retains meaningful capacity across all tested rates, demonstrating a more gradual and recoverable decline.

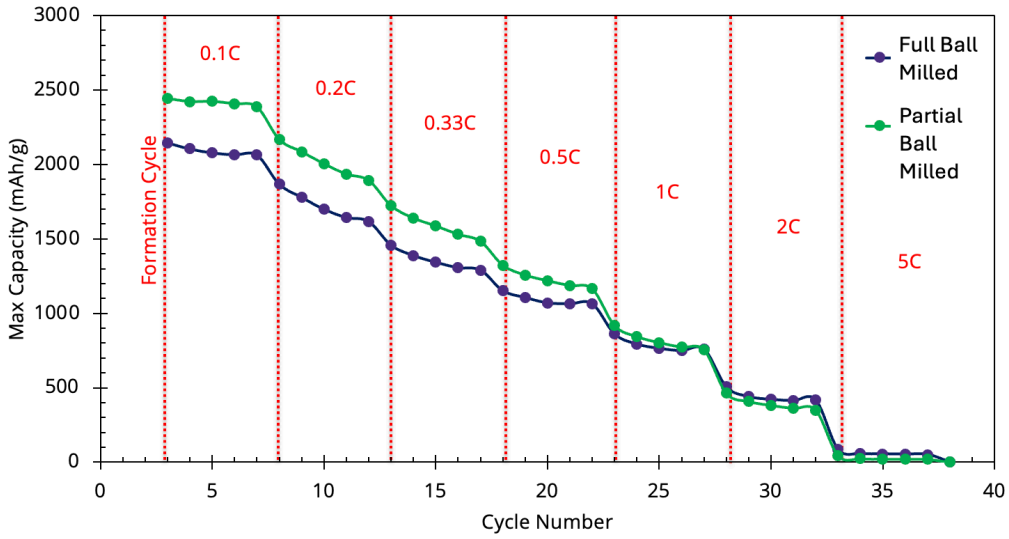

Figure 16 | Maximum specific capacity profiles for Step Mode protocol in each cycle, excluding the first two formation cycles of partial ball milled composite and full ball milled.

This behavior is consistent with the preservation of the high-aspect-ratio CNT network in the partial milling strategy, which provides continuous electron transport pathways that reduce the effective internal resistance under high-drain conditions. The full ball milling method, despite achieving a more homogeneous surface morphology, severs these long-range connections through CNT shortening, leaving the electrode unable to sustain the current demands imposed at elevated rates.

It should be noted that both formulations show near-complete capacity loss at 5C, suggesting that the current electrode architecture and mass loading present a practical upper limit for extreme rate operation. Optimization of mass loading, electrolyte wetting, and porosity will be necessary to extend high-rate performance for aviation applications requiring rapid charge and discharge cycles.

5.3.2 Role of CNTs in Reducing Polarization

The Voltage vs. specific capacity curve in **Figure 16** also provides insight into the internal resistance of the cells. Partial ball milling cell exhibits small graduation even at elevated C-rates compared to full ball milling sample. The voltage gap or polarization of the full ball milling cell battery between the lithiation and delithiation curves widens significantly as the rate increases compared to the partial ball milling, even in some cycles at very high C-rates, the battery hits the voltage cut-off before the silicon can be fully utilized. Hence, the partially ball milling and integration of CNTs strategy suggests that the high-aspect ratio of the CNTs are being preserved, allowing them to maintain a good pathway for the electrons, unlike the full ball milling method.

5.4 Interfacial Stability and Long-Term Capacity Retention

The long-term commercial viability of silicon anodes depends on the formation of a stable SEI. This section evaluates how SiCNT anode with partially ball milling architecture accommodates the mechanical strain of silicon expansion to maintain interfacial stability over extended cycling and reflecting on the capacity of the cells.

5.4.1 Long-Term Cycling Stability

The stability of the partial ball milling strategy is demonstrated across two testing conditions. At 0.1C (**Figure 17(a–b)**), the cell achieved a high initial discharge capacity of approximately 1,700 mAh g^{-1}, maintaining 94.2% capacity retention at cycle 32 and sustaining above 80% capacity retention through cycle 103. This retention can be explained by the web-like CNT network that effectively restrains the silicon particles from electrical isolation during expansion. By contrast, the pure silicon composition in **Figure 15(b)** drops below the 80% threshold at approximately cycle 16, reaching only 69.9% retention by cycle 32. This comparison demonstrates that without the CNT network and the advanced fabrication process, the continuous expansion of silicon particles and a thickening SEI layer will eventually isolate the active material, causing premature failure. Under the 1C long-term cycling condition (**Figure 17(c–d)**), the cell achieved an initial Coulombic efficiency of 94.5% and stabilized Coulombic efficiency of 97.5%

by cycle 75, though capacity retention fell to 11.4% by cycle 1003, also crossing the 80% threshold at cycle 103. The divergence between the 0.1C and 1C retention behavior highlights that while the CNT network effectively sustains interfacial stability at moderate rates, the higher mechanical stress and faster SEI reformation kinetics at 1C accelerate long-term degradation.

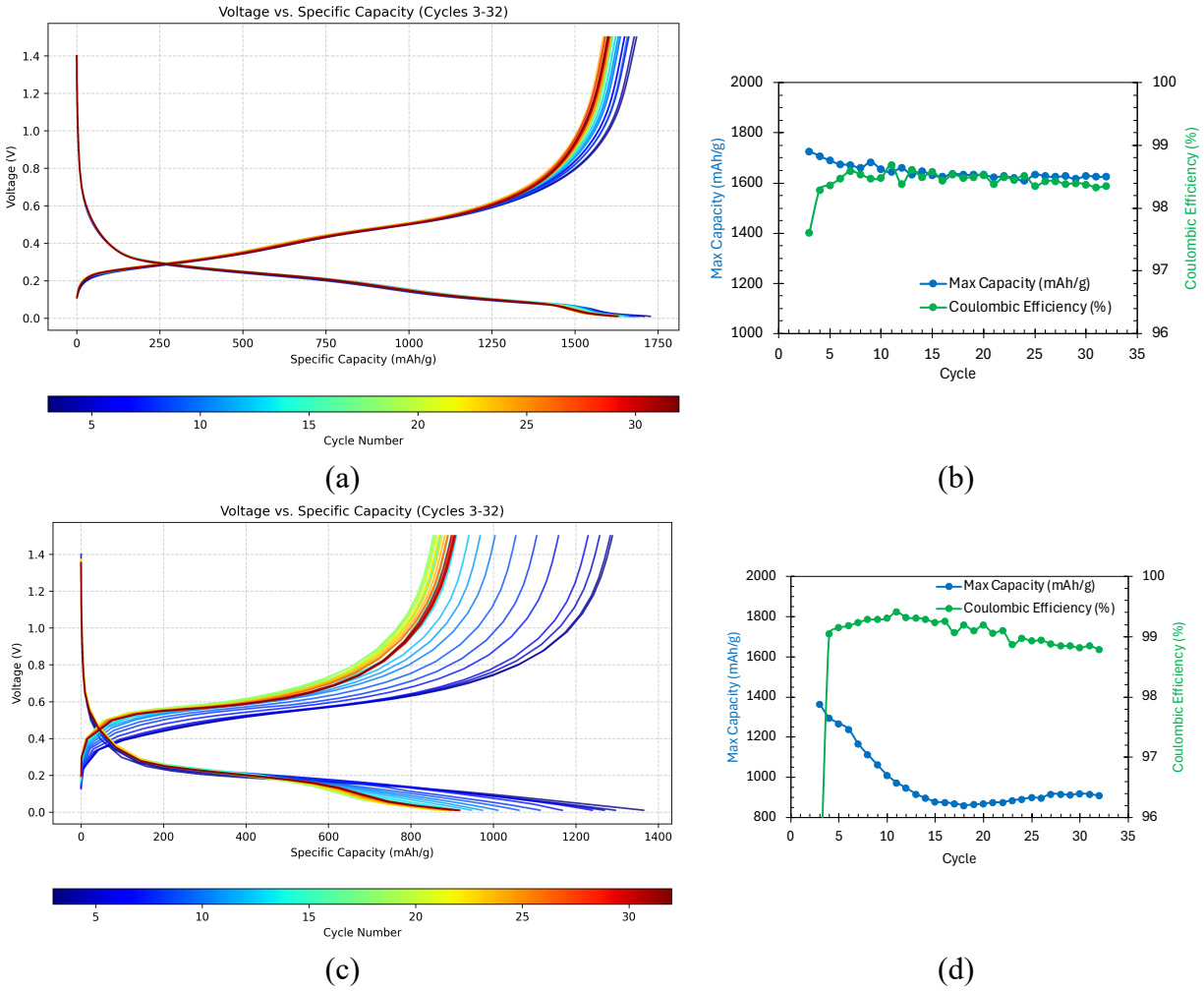

Figure 17 | The Voltage vs. Specific Capacity plot of partial ball milling battery at (a) 0.1C with (b) its coulombic efficiency and capacity and (c) 1C with (d) its coulombic efficiency and capacity, excluding the first two formation cycles.

5.4.2 Coulombic Efficiency and Interface Maturation

Another key indicator of interfacial stability is Coulombic Efficiency (CE), which is the ratio of charge retrieved from a battery during discharging to the charge put in during charging, typically expressed as a percentage that can be calculated using **Equation 1**. As seen in **Figure 18**, the CE of partial ball milling electrode quickly stabilizes after the first two formation cycles. This rapid maturation of the SEI is directly impacted from the optimization of CNT dispersion from the partially milled method that uniformly distributed throughout the structure, rather than agglomerated locally around the silicon's structure. This reduces the continuous consumption of electrolyte, which is also reflecting on the stability of the curve.

Equation 1

$$CE = \frac{Discharge\ Capacity}{Charge\ Capacity} \times 100\%$$

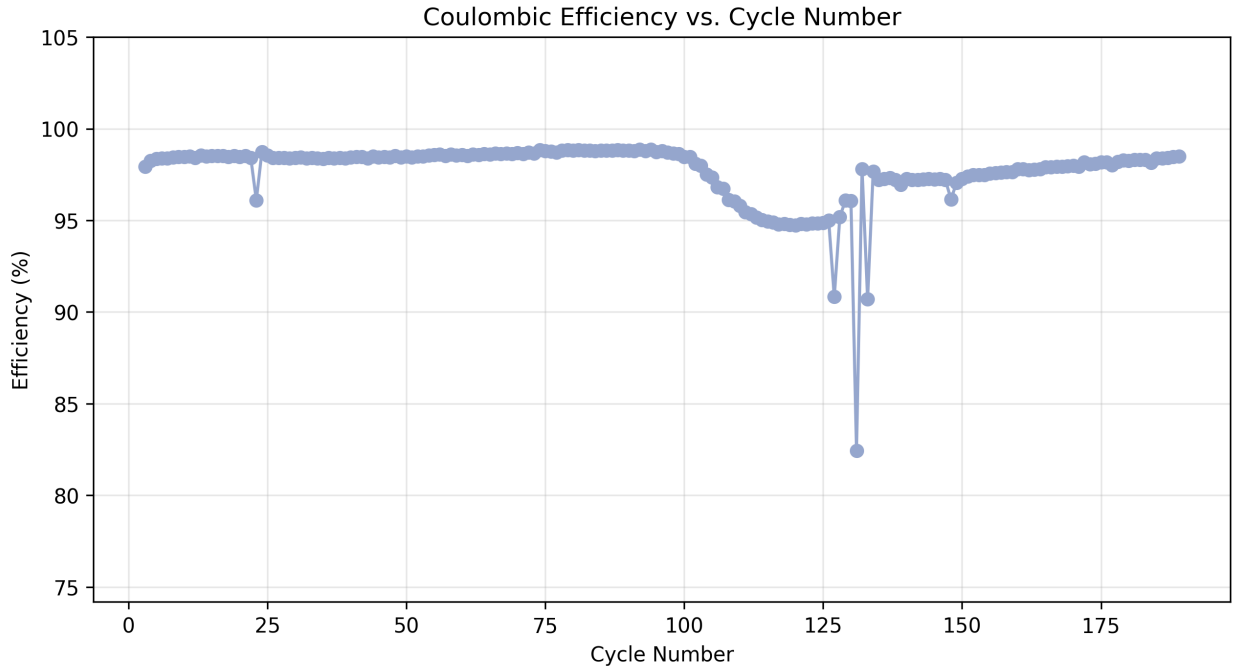

Figure 18 | Coulombic efficiency curve of partial ball milling cell at 0.1C.

5.4.3 Comparative Analysis of the Failure of Full Ball Milling

The most crucial evidence for the validity of the partial ball milled strategy lies in the performance relative to the fully ball milled counterparts. Despite using an identical 6:2:2 material ratio and chemical components, **Figure 19** demonstrated that the fully ball milled method underwent a catastrophic failure, reaching as low as 0.9% retention within the first few cycles. This divergence in performance can be determined from several factors.

The first aspect is the instability of three-phase boundary, namely the active material silicon, the electron conductor CNTs, and the electrolyte. The excessive agglomeration of the nanoparticles severely reduced the availability surface area at the interface where the lithium-ion reaction occurs. The second reason that can cause this failure may from the lack of micro-voids that the CNT network provides. The fully milled composites give the material too homogeneous, causing internal hoop stress of the active material during lithiation and delithiation. Lastly, high-energy full ball milling creates high-energy sites where they are highly reactive and catalyze the decomposition of the electrolyte, leading to thick SEI layer and premature failure.

The over-processed electrode structure also undergoes accelerated electrochemical decay. Despite experiencing a uniform homogenization of active components, the severe structural truncation of the long-range carbon nanotube networks leaves the electrode highly vulnerable to degradation during mechanical breathing. Quantitatively, the full ball milling approach improved short-term stability compared to direct mixing, maintaining a capacity retention of 89.3% at cycle 32 under identical testing parameters. However, due to the severe reduction in the CNT aspect ratio, the network lacks the macro-scale structural resilience required to sustain this performance, leading to structural isolation and an abrupt truncation of usable capacity in subsequent cycles.

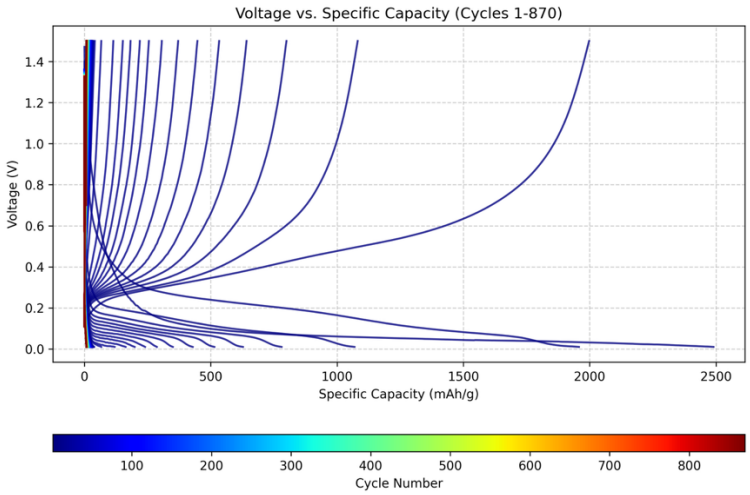

Figure 19 | Voltage vs. Specific Capacity plot of fully ball milled cell.

5.4.4 Three-Way Comparative Performance Summary

To contextualize the electrochemical performance of the partial ball milling strategy, **Figure 20** presents a direct comparison of maximum specific capacity and Coulombic efficiency across all three fabrication approaches — direct mixing, full ball milling, and partial ball milling — over the first 32 post-formation cycles at 0.1C.

In terms of maximum capacity, the direct mixing formulation begins at the highest initial value of approximately 2,150 mAh/g but undergoes the steepest decline, ending near 1,370 mAh/g by cycle 32. The full ball milling approach shows a more moderate initial capacity of approximately 1,820 mAh/g and a more gradual decay, stabilizing near 1,560 mAh/g. The partial ball milling strategy begins at approximately 2,050 mAh/g and shows the most stable trajectory of the three, settling near 1,625 mAh/g by cycle 32 and maintaining the tightest spread between cycles.

The Coulombic efficiency comparison further distinguishes the three approaches. The direct mixing formulation shows the slowest CE maturation, starting near 95.9% and only reaching approximately 98.2% by cycle 32. The full ball milling approach matures more rapidly, stabilizing near 98.3%. The partial ball milling formulation achieves the highest and most stable CE across the tested window, reaching approximately 98.5% and remaining consistently above both comparators from cycle 10 onward.

Taken together, these results confirm that the partial ball milling strategy achieves the best balance between initial capacity, capacity retention stability, and interfacial maturation rate among the three fabrication approaches evaluated in this study. The higher CE of the partial ball milling formulation reflects a more stable and uniform SEI formation enabled by the well-distributed CNT network, while the preserved long-range CNT connectivity accounts for its superior capacity retention relative to the direct mixing baseline.

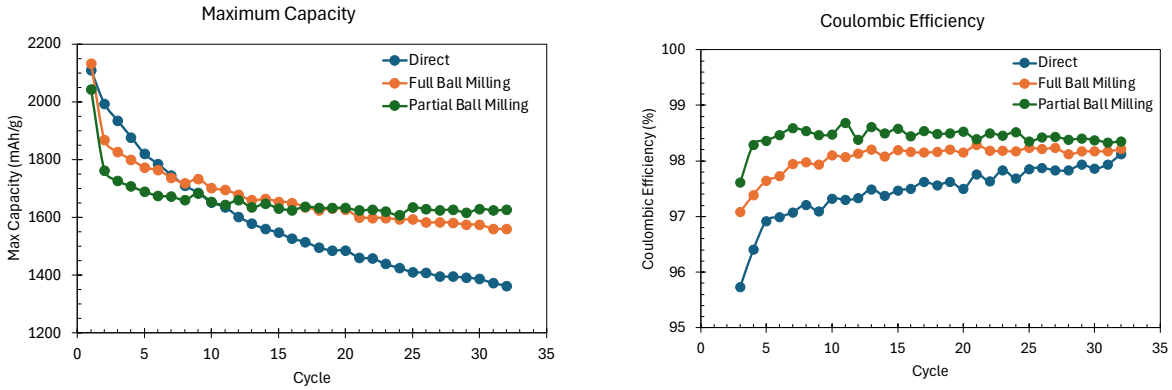

(a) (b)

Figure 20 | Comparison chart of (a) Maximum Capacity and (b) Coulombic Efficiency of Direct Mixing, Full, and Partial Ball Milling.

6. IMPACT

The development of silicon anode battery has driven transformative shift in many industries and aspects which it can be grouped into four main categories. [72] The most significant impact is the enablement of high-energy-density storage application from its ultrahigh theoretical specific capacity. As the traditional graphite offers a capacity of 372 mA h g^{-1}, the silicon has an approximately 11 times the capacity at 3,600 mA h g^{-1}, which this leap is essential for the next-generation LIB to be more practical and long-lasting. The second aspect of the impact is the revolutionization of transportation and consumer electronics industry. The silicon anodes are the answer of range anxiety in electric vehicles (EVs). Typically, the capacity of a production LIB is ~280 W h kg^{-1}, which is notable but often insufficient for long-range travel. [73] By using the next-generation anode with an estimate full-cell capacity at 450 W h kg^{-1}, longer-distance travels with fewer charges are made possible. [74]

To quantify the practical energy density implications of the three fabrication approaches developed in this study, the experimentally measured specific capacities and mass loadings were used to project areal capacities at a standardized mass loading of 2 mg cm^{-2}. At their current experimental mass loadings, the direct mixing, full ball milling, and partial ball milling formulations achieved areal capacities of 1.79, 1.28, and 1.23 mA h cm^{-2}, respectively, reflecting the trade-off between mass loading and specific capacity across the three processing routes. Notably, the partial ball milling approach operates at the lowest mass loading of 0.343 mg cm^{-2}, yet retains a specific capacity of 3,586 mA h g^{-1} — the closest among the three to the direct mixing baseline of 3,609 mA h g^{-1} — demonstrating that the optimized CNT architecture preserves active material utilization even at reduced electrode thickness. When all three formulations are projected to a standardized target loading of 2 mg cm^{-2}, the differences in specific capacity converge, yielding comparable projected areal capacities in the range of 7.11–7.22 mA h cm^{-2}, as summarized in **Table 1**. When further coupled with LFP (3.2 V) and NMC (3.7 V) cathode chemistries and accounting for inactive cell components, these projections translate to real cell-level energy densities of up to 2,295 W h kg^{-1} and 2,653 W h kg^{-1} respectively for the partial ball milling formulation — figures that represent a substantial leap beyond the ~280 W h kg^{-1} practical ceiling of current graphite-based commercial cells, and underscore the viability of this architecture for next-generation high-energy applications.

Table 1 | Comparison of electrochemical performance and projected cell-level energy densities for silicon-based anodes fabricated via direct mixing, full ball milling, and partial ball milling processing routes.

	Specific Capacity (mA h g^{-1})	**Mass Loading (mg cm^{-2})**	**Areal Capacity (mA h cm^{-2})**	**Projected Areal Capacity (mA h cm^{-2})[1]**	**x 0.4V (Half-cell) (W h kg^{-1})[2]**	**x 3.2V (LFP) (W h kg^{-1})[2]**	**x 3.2V (LFP) (W h kg^{-1})[2]**
Direct Mixing	3,609	0.496	1.79	7.22	1,444	2,310	2,671
Full Ball Milling	3,556	0.360	1.28	7.11	1,422	2,276	2,631
Partial Ball Milling	3,586	0.343	1.23	7.17	1,434	2,295	2,653

Furthermore, by 2035, the EV market share is projected to be 42.5% worldwide and the Si-based anodes are key to meet this growing demand for longer-lasting and powerful batteries. [75] In the area of consumer electronics, silicon anodes have become a necessity for AI-enabled smartphones. [76] These devices require high computing power, especially for on-device processing, and these new batteries offer energy density to support these features without increasing the size of the devices. Additionally, the Aerospace sector is also leveraging high energy density silicon anode for eVTOL (electric Vertical Take-off and Landing) aircraft that meet the demanding flight requirements for zero emission transportations. [77] The next sector is the sustainability and economic availability, of which silicon offers sustainable resource option compared to scarcer rare earth metals. The silicon also classified as an environmentally friendly material with a low working potential to lithium and lower energy cost potential. [78] Safety aspect of the battery also faces a major improvement from using silicon as the main anode in the solid-state batteries (SSB). [79] The SSBs replace liquid electrolyte with inorganic solid electrolytes, offering a wider electrochemical stability window.

[1] Projected metrics assume a target mass loading scaled to 2 mg cm^{-2}.
[2] Projected metrics assume a cell-level reduction factor of 5 to account for inactive components and typical practical densities.

7. FUTURE WORK

Although the aforementioned results have the potential to yield significant results, future testing, optimization, and in-depth data analysis with higher confidence level are required prior the commercialization of this battery for aviation that has high energy density that is capable for high C-rate.

In the aviation industry, safety is one if not the top priorities that is intolerable to compromises. In this work, the focus is mainly on the improvement of energy density over the standard silicon anode, future work must address how these cells behave under the operating environment or extreme conditions. The aviation standards demand a fail-safe mechanism which can be translated as a single cell failure would not lead to an overall catastrophic event. Future research should focus on the thermal propagation of the battery to study its thermal runaway behavior that includes nail penetration experiment, both in single and multiple cell configurations, to observe the heat propagation of each cell. An investigation of a new type of electrolyte that is non-flammable solid-state type or at least a flame-retardant additive would also be beneficial to minimize the risk of fire. Aircraft batteries are subject to environmental extremes that are rarely captured in a controlled laboratory setting.

The illustration of **Table 2** shows the demanding cycle life requirements imposed by commercial aviation. Short-haul aircraft such as the Airbus A320 and Boeing 737 accumulate between 1,200 and 1,800 cycles annually over a service life of 25-30 years, implying a total requirement of 30,000-54,000 battery cycles. Regional aircraft operating shorter hops face even higher annual cycle counts of up to 2,500. These figures underscore that battery systems intended for aviation must far exceed the cycle life demonstrated in laboratory half-cell testing, and that future work must focus on closing this gap through full-cell validation, accelerated aging protocols, and battery management systems capable of predicting end-of-life under real operational conditions. The battery not only required to withstand the internal failure from normal operating cycles, but also many external operating conditions that the aircraft should tolerate, like pressure and altitude cycling. The electrochemical performance under rapid decompression and low ambient pressures to ensure casing integrity and stable ion transportation. Furthermore, mechanical vibration under normal operating circumstances can lead to contact loss at the electrode-current collector interface. Testing the vibration can further reflect a realistic aging profile of the battery.

Table 2 | Estimated Service Life by Aircraft Type. **[80–82]**

Flight Type	Aircraft Examples	Typical Annual Hours	Typical Annual Cycles	Average Flight Duration (Hours)	Lifetime Limit (Hours / Cycles)	Estimated Time until Retirement (Years)
Short-Haul (Narrow-body)	Airbus A320, Boeing 737	2,800 – 3,200	1,200 – 1,800	1.5 – 2.5	75,000 / 45,000	~25 – 30
Long-Haul (Wide body)	Airbus A350, Boeing 777, 787	4,000 – 5,000	300 – 600	8 – 12+	90,000 / 25,000	~20
Regional (Short-Hops)	Embraer 175, Bombardier CRJ	2,000 – 2,500	2,000 – 2,500	0.75 – 1.5	60,000 / 60,000	~25

The cycle life demonstrated in this study — 1,000 charge-discharge cycles under laboratory half-cell conditions — represents a small fraction of the operational demands outlined in Table 1. Short-haul narrowbody aircraft such as the Airbus A320 accumulate an estimated 30,000 to 54,000 battery cycles over a 25–30-year service life, while regional aircraft operating short-hop routes may require up to 60,000 cycles. The present work therefore serves as a proof-of-concept for the partial ball milling architecture rather than a demonstration of aviation-ready cycle life. Closing this gap will require a multi-stage validation pathway: full-cell testing to eliminate the excess lithium reservoir inherent to half-cell configurations, accelerated ageing protocols designed around aviation duty cycles, and integration with a battery management system capable of real-time state-of-health estimation. Each of these steps introduces degradation mechanisms not captured in the current half-cell protocol, and their cumulative effect on the partial ball milling electrode architecture remains an open research question that constitutes the primary target of future work.

To get a better understanding of the degradation mechanism of the battery, the utilization of X-Ray using In-Operando X-Ray Tomography to get a real-time visualization of electrode expansion and pulverization during lithiation process. [83] Another analysis that should be made is the SEI analysis which employs Cryogenic Scanning Electron Microscopy to gain a better understanding of the failure mechanism, stableness, and the true thickness of the SEI layer. [84]

Lastly, to fully integrate the battery into the aviation application, the battery must be paired with its own battery management system (BMS) to ensure a reliable and long-lasting operation. By developing a machine learning model to predict the life of the battery will be critical for scheduling maintenance. Furthermore, an optimization for fast-charging or extreme fast-charging protocols is essential to reduce ground turnaround times without accelerating the degradation of the battery.

8. CONCLUSION

This study has successfully demonstrated that the structural and electrochemical limitations of silicon-based anodes can be effectively mitigated through a specialized partial ball milling fabrication strategy. By integrating multi-walled carbon nanotubes (MWCNTs) into the silicon matrix using a 70/30 hybrid approach — where 70% of the total CNT weight was high-energy ball-milled for dispersion and the remaining 30% was standard-mixed to preserve high aspect ratio properties — this research established a robust electrode architecture capable of withstanding the extreme volumetric changes inherent to silicon lithiation.

The morphological characterization of the silicon electrode confirmed that this dual-stage processing greatly avoids the drawbacks of direct mixing, which promotes agglomeration of both silicon nanoparticles and CNTs, and avoids the mechanical degradation of CNT length and structural strength that results from full ball milling. This optimized partial ball milling process yields two key structural advantages: a dense, uniform matrix providing localized electrical contact, and a long-range interwoven CNT network that acts as a tensile buffer during silicon lithiation up to 300% volumetric expansion.

Electrochemical testing validated the performance of this architecture across three fabrication methods. Under initial 0.1C evaluation protocols, the direct mixing baseline achieved an ICE of 82.6%, while the full ball milling approach yielded 82.7%. The full ball milling approach improved retention to 89.3% at cycle 32 with an ICE of 82.7% but suffered from a degraded conductive network and poor substrate adhesion due to CNT shortening. The optimized partial ball milling anode achieved the best overall performance, with 94.2% capacity retention at cycle 32, maintaining above 80% capacity retention through cycle 103 at 0.1C. Under the 1C long-term cycling condition, the cell reached a high initial Coulombic efficiency of 94.5% and stabilized Coulombic efficiency of 97.5% by cycle 75. Under high-drain conditions up to 5C, the partial ball milling electrode maintained meaningful capacity across all C-rates, outperforming the full ball milling control, consistent with the preservation of the high-aspect-ratio CNT network maintaining efficient electron transport pathways.

When the electrochemical performance is contextualized against practical energy density targets, the significance of this architecture becomes further apparent. At their current experimental mass loadings, the direct mixing, full ball milling, and partial ball milling formulations achieved areal capacities of 1.79, 1.28, and 1.23 mA h cm^{-2}, respectively. While the partial ball milling approach operates at the lowest experimental mass loading of 0.343 mg cm^{-2}, it retains a specific capacity of 3,586 mA h g^{-1} — the closest among the three to the direct mixing baseline of 3,609 mA h g^{-1} — demonstrating that the optimized CNT architecture preserves active material utilization even at reduced electrode thickness. When all three formulations are projected to a standardized target loading of 2 mg cm^{-2}, the differences in specific capacity converge to yield comparable projected areal capacities in the range of 7.11–7.22 mA h cm^{-2}. When further coupled with LFP (3.2 V) and NMC (3.7 V) cathode chemistries and accounting for inactive cell

components, these projections translate to real cell-level energy densities of up to 2,295 W h kg^{-1} and 2,653 W h kg^{-1} respectively for the partial ball milling formulation — figures that substantially exceed the ~280 W h kg^{-1} practical ceiling of current graphite-based commercial cells. Critically, these projections suggest that further optimization of electrode thickness at standardized loading conditions could close the marginal areal capacity gap relative to direct mixing, while preserving the superior cycling stability and interfacial maturation that define the electrochemical advantage of the partial ball milling strategy.

In conclusion, the integration of structural reinforcement through optimized CNT dispersion provides a viable path toward high-energy density, long-lasting silicon anodes. The partial ball milling strategy successfully balances the trade-off between local electrical contact and long-range mechanical integrity, and the electrode architecture has demonstrated potential to meet the requirements for regional-range electric aviation applications while reducing reliance on critical minerals by leveraging silicon's natural abundance.

REFERENCES

1. Sudduth, W.M.: The voltaic pile and electro-chemical theory in 1800. Ambix. 27, 26–35 (1980)
2. Li, M., Lu, J., Chen, Z., Amine, K.: 30 years of lithium-ion batteries. Advanced materials. 30, 1800561 (2018)
3. Yoshino, A.: The birth of the lithium-ion battery. Angewandte Chemie International Edition. 51, 5798–5800 (2012)
4. Li, Q., Yang, Y., Yu, X., Li, H.: A 700 W· h· kg− 1 rechargeable pouch type lithium battery. Chinese Physics Letters. 40, 048201 (2023)
5. Khan, F.M.N.U., Rasul, M.G., Sayem, A.S.M., Mandal, N.: Maximizing energy density of lithium-ion batteries for electric vehicles: A critical review. Energy Reports. 9, 11–21 (2023). https://doi.org/10.1016/j.egyr.2023.08.069
6. Gkyrtis, K.: The Impact of Weight Distribution in Heavy Battery Electric Vehicles on Pavement Performance: A Preliminary Study. World Electric Vehicle Journal. 16, 520 (2025). https://doi.org/10.3390/wevj16090520
7. Fischer, M., Werber, M., Schwartz, P.V.: Batteries: Higher energy density than gasoline? Energy Policy. 37, 2639–2641 (2009). https://doi.org/10.1016/j.enpol.2009.02.030
8. Muttana, S.B., Sardar, A.: Lightweighting of battery electric cars: an impact analysis using Indian driving cycle. SAE Technical Paper (2013)
9. Berjoza, D., Jurgena, I.: Effects of change in the weight of electric vehicles on their performance characteristics. Agronomy Research. 15, (2017)
10. Lučić, M., Lukić, J., Grujic, I.: Statistical analysis of trends in Battery Electric Vehicles: Special reference to vehicle weight reduction, electric motor, battery, and interior space dimensions. The Archives of Automotive Engineering–Archiwum Motoryzacji. (2024)
11. Wang, Q., Ping, P., Zhao, X., Chu, G., Sun, J., Chen, C.: Thermal runaway caused fire and explosion of lithium ion battery. Journal of power sources. 208, 210–224 (2012)
12. Zeng, X., Li, J., Liu, L.: Solving spent lithium-ion battery problems in China: Opportunities and challenges. Renewable and Sustainable Energy Reviews. 52, 1759–1767 (2015)
13. McManus, M.C.: Environmental consequences of the use of batteries in low carbon systems: The impact of battery production. Applied Energy. 93, 288–295 (2012)
14. Buratovic, E., Cocalic, D., Eliasson, K., Danestig, M., Everlid, L.: Controversial Materials: Ethical issues in the production of mineral based raw materials. (2017)
15. Ren, H., Mu, D., Wang, C., Yue, X., Li, Z., Du, J., Zhao, L., Lim, M.K.: Vulnerability to geopolitical disruptions of the global electric vehicle lithium-ion battery supply chain network. Computers & Industrial Engineering. 188, 109919 (2024)
16. Xu, M., David, J.M., Kim, S.H.: The fourth industrial revolution: Opportunities and challenges. International journal of financial research. 9, 90–95 (2018)
17. Krepelková, M.: Evolution of batteries: From experiments to everyday usage. Presented at the 21th International Student Conference on Electrical Engineering (2017)
18. Mills, A.A.: Early voltaic batteries: An evaluation in modern units and application to the work of Davy and Faraday. Annals of science. 60, 373–398 (2003)
19. Decker, F.: Volta and the pile. Electrochemistry Encyclopedia. (2005)
20. Pavlov, D.: Lead-acid batteries: science and technology. Elsevier (2011)
21. Ghavami, R.K., Rafiei, Z.: Performance improvements of alkaline batteries by studying the effects of different kinds of surfactant and different derivatives of benzene on the electrochemical properties of electrolytic zinc. Journal of Power Sources. 162, 893–899 (2006)

22. Chen, W., Chen, T., Fu, J.: Pivotal role of organic materials in aqueous zinc-based batteries: regulating cathode, anode, electrolyte, and separator. Advanced Functional Materials. 34, 2308015 (2024)
23. Bernard, P., Lippert, M.: Nickel–cadmium and nickel–metal hydride battery energy storage. In: Electrochemical energy storage for renewable sources and grid balancing. pp. 223–251. Elsevier (2015)
24. Aktaş, A., Kirçiçek, Y.: Solar Hybrid Systems: Design and Application. Academic Press (2021)
25. Li, M., Lu, J., Chen, Z., Amine, K.: 30 years of lithium-ion batteries. Advanced materials. 30, 1800561 (2018)
26. Whittingham, M.S., Yoshino, A.: Lithium-Ion Batteries. The Royal Swedish Academy of Sciences. (2019)
27. Suslov, E.A., Bushkova, O.V., Sherstobitova, E.A., Reznitskikh, O.G., Titov, A.N.: Lithium intercalation into TiS2 cathode material: phase equilibria in a Li–TiS2 system. Ionics. 22, 503–514 (2016)
28. Monroe, D.: Building a better battery. (2020)
29. Mizushima, K., Jones, P.C., Wiseman, P.J., Goodenough, J.B.: LixCoO2 (0< x<-1): A new cathode material for batteries of high energy density. Materials Research Bulletin. 15, 783–789 (1980)
30. Padhi, A.K., Nanjundaswamy, K.S., Goodenough, J.B.: Phospho-olivines as positive-electrode materials for rechargeable lithium batteries. Journal of the electrochemical society. 144, 1188 (1997)
31. Xie, J., Lu, Y.-C.: A retrospective on lithium-ion batteries. Nature communications. 11, 2499 (2020)
32. Wani, T.A., Suresh, G.: A comprehensive review of LiMnPO4 based cathode materials for lithium-ion batteries: current strategies to improve its performance. Journal of Energy Storage. 44, 103307 (2021)
33. Bubulinca, C., Kazantseva, N.E., Pechancova, V., Joseph, N., Fei, H., Venher, M., Ivanichenko, A., Saha, P.: Development of all-solid-state Li-ion batteries: From key technical areas to commercial use. Batteries. 9, 157 (2023)
34. Johnson, C.S., Li, N., Lefief, C., Thackeray, M.M.: Anomalous capacity and cycling stability of xLi2MnO3·(1− x) LiMO2 electrodes (M= Mn, Ni, Co) in lithium batteries at 50° C. Electrochemistry Communications. 9, 787–795 (2007)
35. Chang, L., Yang, W., Cai, K., Bi, X., Wei, A., Yang, R., Liu, J.: A review on nickel-rich nickel–cobalt–manganese ternary cathode materials LiNi0.6Co0.2Mn0.2O2 for lithium-ion batteries: performance enhancement by modification. Mater. Horiz. 10, 4776–4826 (2023). https://doi.org/10.1039/D3MH01151H
36. Jung, R., Metzger, M., Maglia, F., Christoph, S., Hubert, G.: Oxygen release and its effect on the cycling stability of LiNixMnyCozO2 (NMC) cathode materials for Li-ion batteries. Journal of the electrochemical society.
37. Shi, X.-H., Wang, Y.-P., Cao, X., Wu, S., Hou, Z., Zhu, Z.: Charge compensation mechanisms and oxygen vacancy formations in LiNi1/3Co1/3Mn1/3O2: first-principles calculations. ACS omega. 7, 14875–14886 (2022)
38. Li, T., Yuan, X.-Z., Zhang, L., Song, D., Shi, K., Bock, C.: Degradation mechanisms and mitigation strategies of nickel-rich NMC-based lithium-ion batteries. Electrochemical Energy Reviews. 3, 43–80 (2020)

39. RN, R., Bosubabu, D., MG, K.B., Ramesha, K.: Tuning of Ni, Mn, and Co (NMC) content in 0.4 (LiNi x Mn y Co z O2)· 0.4 (Li2MnO3) toward stable high-capacity lithium-rich cathode materials. ACS Applied Energy Materials. 3, 10872–10881 (2020)
40. Abebe, E.B., Yang, C.-C., Wu, S.-H., Chien, W.-C., Li, Y.-J.J.: Effect of Li excess on electrochemical performance of Ni-rich LiNi0. 9Co0. 05Mn0. 05O2 cathode materials for Li-ion batteries. ACS Applied Energy Materials. 4, 14295–14308 (2021)
41. Itani, K., De Bernardinis, A.: Review on new-generation batteries technologies: trends and future directions. Energies. 16, 7530 (2023)
42. Zhang, H., Yang, Y., Ren, D., Wang, L., He, X.: Graphite as anode materials: Fundamental mechanism, recent progress and advances. Energy Storage Materials. 36, 147–170 (2021)
43. Liang, B., Liu, Y., Xu, Y.: Silicon-based materials as high capacity anodes for next generation lithium ion batteries. Journal of Power sources. 267, 469–490 (2014)
44. Cisco, G.: Strategic opportunity or a chokepoint in disguise?: the case of silicon-anodes in the European battery supply chain. (2025)
45. Lee, T., Seong, M.J., Ahn, H.C., Baek, M., Park, K., Oh, J., Choi, T., Choi, J.W.: Fast-chargeable lithium-ion batteries by μ-Si anode-tailored full-cell design. Proceedings of the National Academy of Sciences. 122, e2417053121 (2025). https://doi.org/10.1073/pnas.2417053121
46. Kim, I., Kang, H., Yoon, S., Lee, J.B., Kim, H.W., Kim, H.-K., Kim, M.: A design guideline of graphite/silicon composite electrode for extremely fast charging Li ion batteries. Energy Storage Materials. 72, 103739 (2024)
47. Senyshyn, A., Mühlbauer, M., Dolotko, O., Ehrenberg, H.: Low-temperature performance of Li-ion batteries: The behavior of lithiated graphite. Journal of Power Sources. 282, 235–240 (2015)
48. Zhu, J., Wang, T., Fan, F., Mei, L., Lu, B.: Atomic-scale control of silicon expansion space as ultrastable battery anodes. ACS nano. 10, 8243–8251 (2016)
49. Ramdhiny, M.N., Jeon, J.: Design of multifunctional polymeric binders in silicon anodes for lithium-ion batteries. Carbon Energy. 6, e356 (2024)
50. Zheng, Z., Liu, Z., Wang, P., Li, Y.: Numerical modeling on the delamination-induced capacity degradation of silicon anode. Journal of Energy Storage. 43, 103190 (2021)
51. Je, M., Han, D.-Y., Ryu, J., Park, S.: Constructing pure Si anodes for advanced lithium batteries. Accounts of Chemical Research. 56, 2213–2224 (2023)
52. Rowden, B., Garcia-Araez, N.: Estimating lithium-ion battery behavior from half-cell data. Energy Reports. 7, 97–103 (2021)
53. Chen, X., Cheng, W., Liu, H., Chen, H., Ma, J., Zhang, Y., Wu, Z., Wang, C., You, Y., Xing, X., Wu, Z.: Research Progresses on Nano-Structured Silicon-Based Materials as Anode for Lithium-Ion Batteries. Materials (Basel). 18, 830 (2025). https://doi.org/10.3390/ma18040830
54. Popov, V.N.: Carbon nanotubes: properties and application. Materials Science and Engineering: R: Reports. 43, 61–102 (2004)
55. Xu, L., Yang, J., Yuan, X., Chen, L., Chen, M.: Efficient synthesis of high quality double walled carbon nanotubes and their cost-effective properties. New Journal of Chemistry. 46, 18724–18731 (2022)
56. Kukovecz, Á., Kozma, G., Kónya, Z.: Multi-walled carbon nanotubes. In: Springer handbook of nanomaterials. pp. 147–188. Springer (2013)
57. Andrews, R., Jacques, D., Qian, D., Rantell, T.: Multiwall carbon nanotubes: synthesis and application. Accounts of chemical research. 35, 1008–1017 (2002)

58. Zhang, Y., Zhang, X., Zhang, H., Zhao, Z., Li, F., Liu, C., Cheng, H.: Composite anode material of silicon/graphite/carbon nanotubes for Li-ion batteries. Electrochimica acta. 51, 4994–5000 (2006)
59. Mo, T., Li, Y., Zhao, H.: The Utilization of Carbon Nanotubes in Advanced Silicon – Carbon Anode Materials for Lithium-Ion Batteries. In: Carbon Nanotubes - Recent Advances, Perspectives and Applications. IntechOpen (2024)
60. Tzeng, Y., Jhan, C.-Y., Wu, Y.-C., Chen, G.-Y., Chiu, K.-M., Guu, S.Y.-E.: High-ICE and High-Capacity Retention Silicon-Based Anode for Lithium-Ion Battery. Nanomaterials. 12, 1387 (2022). https://doi.org/10.3390/nano12091387
61. Parikh, P., Sina, M., Banerjee, A., Wang, X., D'Souza, M.S., Doux, J.-M., Wu, E.A., Trieu, O.Y., Gong, Y., Zhou, Q.: Role of polyacrylic acid (PAA) binder on the solid electrolyte interphase in silicon anodes. Chemistry of Materials. 31, 2535–2544 (2019)
62. Zhong, L., Sun, Y., Shen, K., Li, F., Liu, H., Sun, L., Xie, D.: Poly (Acrylic Acid)-Based Polymer Binders for High-Performance Lithium-Ion Batteries: From Structure to Properties. Small. 20, 2407297 (2024)
63. Yi, W., Zhao, T., Li, D., Yuan, Q., Zhao, Z., Chen, B., Dang, N.: Research Progress of Polyacrylate Binders for Silicon-Based Anodes in Lithium-Ion Batteries. Chemistry–A European Journal. 31, e202500321 (2025)
64. Zhu, R., Liu, S., Li, T., Yang, D.: Precisely prelithiated polyacrylic acid binder improving electrochemical performance of micron-sized silicon anodes for lithium-ion batteries. ChemElectroChem. 11, e202400326 (2024)
65. Martin, T.R., Pekarek, R.T., Coyle, J.E., Schulze, M.C., Neale, N.R.: Understanding why poly (acrylic acid) works: decarbonylation and cross-linking provide an ionically conductive passivation layer in silicon anodes. Journal of Materials Chemistry A. 9, 21929–21938 (2021)
66. Li, H., Wang, L., Song, Y., Zhang, Z., Zhang, H., Du, A., He, X.: Significance of current collectors for high performance conventional lithium-ion batteries: a review. Advanced Functional Materials. 33, 2305515 (2023)
67. Liu, Y., Gao, D., Xiang, H., Feng, X., Yu, Y.: Research progress on copper-based current collector for lithium metal batteries. Energy & Fuels. 35, 12921–12937 (2021)
68. Xu, Z., Yang, J., Li, H., Nuli, Y., Wang, J.: Electrolytes for advanced lithium ion batteries using silicon-based anodes. Journal of Materials Chemistry A. 7, 9432–9446 (2019)
69. Foundation, V.: Lithium-ion Battery Separators and their Role in Safety, https://volta.foundation/battery-bits/lithium-ion-battery-separators-and-their-role-in-safety, (2021)
70. Battery Separator Products & Literature | Celgard World Leader in Battery Separator Technology, https://www.celgard.com/product-data
71. An, S.J., Li, J., Du, Z., Daniel, C., Wood III, D.L.: Fast formation cycling for lithium ion batteries. Journal of Power Sources. 342, 846–852 (2017)
72. Sun, L., Liu, Y., Shao, R., Wu, J., Jiang, R., Jin, Z.: Recent progress and future perspective on practical silicon anode-based lithium ion batteries. Energy Storage Materials. 46, 482–502 (2022)
73. Khan, F.N.U., Rasul, M.G., Sayem, A., Mandal, N.: Maximizing energy density of lithium-ion batteries for electric vehicles: A critical review. Energy Reports. 9, 11–21 (2023)
74. Li, B., Gao, X., Li, J., Yuan, C.: Life cycle environmental impact of high-capacity lithium ion battery with silicon nanowires anode for electric vehicles. Environmental science & technology. 48, 3047–3055 (2014)

75. Rietmann, N., Hügler, B., Lieven, T.: Forecasting the trajectory of electric vehicle sales and the consequences for worldwide CO2 emissions. Journal of cleaner production. 261, 121038 (2020)
76. Mahalakshmi, B., Ananthi, K., Palpandian, P., Balachander, K.: The Evolution of Smartphone Battery Technology: From the First Mobile Phone to Modern-Day Devices and Future Advancements. International Research Journal of Multidisciplinary Technovation. 7, 1–12 (2025)
77. Barrera, T.P., Bond, J.R., Bradley, M., Gitzendanner, R., Darcy, E.C., Armstrong, M., Wang, C.-Y.: Next-generation aviation Li-ion battery technologies—Enabling electrified aircraft. The Electrochemical Society Interface. 31, 69 (2022)
78. Jia, T., Zhong, G., Lv, Y., Li, N., Liu, Y., Yu, X., Zou, J., Chen, Z., Peng, L., Kang, F.: Prelithiation strategies for silicon-based anode in high energy density lithium-ion battery. Green Energy & Environment. 8, 1325–1340 (2023)
79. Huo, H., Janek, J.: Silicon as emerging anode in solid-state batteries. ACS Energy Letters. 7, 4005–4016 (2022)
80. The Complex Art of Aircraft Utilization, https://www.airwaysmag.com/legacy-posts/art-of-aircraft-utilization
81. Life Span of an Airplane? | JE Technology Solutions, https://jetechnologysolutions.com/resources/life-span-of-an-airplane/
82. These Were The Most Used Commercial Aircraft Types In 2022, https://simpleflying.com/most-used-commercial-aircraft-types-2022/
83. Tariq, F., Yufit, V., Eastwood, D.S., Merla, Y., Biton, M., Wu, B., Chen, Z., Freedman, K., Offer, G., Peled, E., Lee, P.D., Golodnitsky, D., Brandon, N.: In-Operando X-ray Tomography Study of Lithiation Induced Delamination of Si Based Anodes for Lithium-Ion Batteries. ECS Electrochem. Lett. 3, A76 (2014). https://doi.org/10.1149/2.0081407eel
84. Wang, J., Wang, D.: Cryo-EM Reveals the Structure and Chemistry of the Silicon Solid-Electrolyte Interphase. Chem. 6, 331–334 (2020). https://doi.org/10.1016/j.chempr.2020.01.006